The Sensitivity of Multiangle Imaging to Natural Mixes of Aerosols Over Ocean

Ralph Kahn, Pranab Banerjee, and Duncan McDonald

Jet Propulsion Laboratory, California Institute of Technology

4800 Oak Grove Drive, Pasadena CA 91109

Submitted to: The Journal of Geophysical Research, Atmospheres

November, 1999

Abstract

Multiangle, multispectral remote sensing observations, such as those anticipated from the Earth Observing System (EOS) Multi-angle Imaging SpectroRadiometer (MISR), can significantly improve our ability to constrain aerosol properties from space. Earlier theoretical studies explored the sensitivity of MISR to aerosol properties [*Kahn et al.*, 1997; 1998] based on a "generic" retrieval approach; top-of-atmosphere radiances were interpreted in terms of a single, average aerosol population having unimodal size distribution and uniform composition. MISR can distinguish about a dozen groupings of particles over the natural range of physical properties: 3 sizes, 2 to 3 compositions, and spherical vs. randomly oriented nonspherical particles. This work is extended using a "climatological" retrieval approach that asks how well MISR can distinguish among assumed, climatologically likely, external mixtures of particle types. A simplified climatology containing 5 Mixing Groups, each composed of all possible combinations of 4 particle type end-members, is abstracted from published aerosol transport model results. With the additional assumptions, the ability to distinguish among air masses containing common mixtures of atmospheric aerosols with MISR data is assessed.

Results are based on theoretical simulations under good viewing conditions, for retrievals using all 9 MISR angles and the 2 wavelengths least affected by ocean surface reflectance. MISR can distinguish fractional optical depths of climatologically likely mixtures containing large, spherical particles (Sea Salt), non-spherical particles (Accumulation and Coarse Mode Dust), and small, dark particles (Black Carbon), to within 20% or better of the expected values. MISR is not good at distinguishing medium, spherical, non-absorbing (Sulfate) from medium, spherical, absorbing (Carbonaceous) particles, but the sum is retrieved to within 20% or better.

MISR is also able to distinguish thin cirrus from other particle types in the climatology if the total column aerosol optical depth is greater than about 0.2 and the cirrus contribution is more than about 20%. The ability of MISR to identify aerosol Air Mass Types is significantly reduced when cirrus is present, or if the overall aerosol optical depth is low, but the sensitivity to total aerosol optical depth is not diminished. We expect the MISR data, with its frequent global coverage, to complement *in situ* and field data, which can provide more detailed information about aerosol size and composition locally. This combined effort should advance our knowledge of aerosol behavior globally, and our ability to model the impact of aerosols on the climatically important solar radiation budget.

1. Introduction

Recent advances in modeling Earth's climate and studying its radiation balance have brought us to a point where the contributions made by aerosols to the global radiation budget significantly affect the results [e.g., *Andreae*, 1995; *Charlson et al.*, 1992; *Cusack et al.*, 1998; *Hansen et al.*, 1997; *Haywood et al.*, 1999; *Li et al.*, 1997; *Penner et al.*, 1994]. Aerosols are thought to contribute to direct radiative forcing in the atmosphere, and indirectly, through their influence as nucleation sites for cloud particles. Knowledge of both aerosol optical depth and the microphysical properties of particles are needed to adequately model aerosol effects.

Currently, we must rely on satellite remote sensing to provide the spatial and temporal coverage required for global monitoring of atmospheric aerosols. However, the retrieval of aerosol properties by remote sensing is a notoriously under-determined problem. And the only operational, global-scale, satellite-based retrieval of aerosols derives aerosol optical depth from single-angle, monospectral data, using assumed values for all the aerosol microphysical properties [*Rao et al.*, 1989; *Stowe et al.*, 1997].

Multiangle, multispectral remote sensing observations, such as those anticipated from the Earth Observing System (EOS) Multiangle Imaging SpectroRadiometer (MISR), provide a type of information about the characteristics of aerosols never before obtained from satellites [*Martonchik et al.*, 1998; *Diner et al.*, 1998a]. MISR is scheduled for launch into polar orbit on the EOS AM-1 platform in 1999. It will measure the upwelling short-wave radiance from Earth in 4 spectral bands centered at 446, 558, 672, and 866 nm, at each of 9 view angles spread out in the forward and aft directions along the flight path at 70.5°, 60.0°, 45.6°, 26.1°, and nadir. The maximum spatial sampling rate is 275 meters in the cross-track and along-track directions, at all angles except nadir, where the cross-track sampling is 250 meters. Over a period of 7 minutes, a 360 km wide swath of Earth comes into the view of the cameras at each of the 9 emission angles, providing a wide range of scattering angle coverage for each surface location. Complete coverage of latitude bands will take 9 days at the equator and 2 days in polar regions; the nominal mission lifetime is 6 years.

MISR data will be used to characterize surface albedo and bi-directional reflectance, and cloud properties. We also plan to retrieve aerosol optical depth, and to distinguish as well as possible air masses containing different mixes of particles, globally, at 17.6 km spatial resolution.

This is the third in a series of papers that explores our ability to retrieve information about atmospheric aerosols from MISR. The first two papers [*Kahn et al.*, 1997; 1998] ask how well we can distinguish pure particle types having different size distributions, indices of refraction, optical depths, and spherical or non-spherical shapes. This "generic" approach to aerosol retrieval interprets top-of-atmosphere radiances in terms of a cross-section-mean-weighted effective aerosol population having unimodal, lognormal size distribution and uniform composition. Based on the simulations, we show that over calm ocean surfaces, and with commonly observed ranges of particle optical depth and size distribution, MISR can retrieve column optical depth for all but the darkest particles, to an accuracy better than 0.05 or 20%, whichever is larger, even if the microphysical properties of the particles are poorly known. It can distinguish spherical from non-spherical particles having Sahara dust-like composition. At most latitudes, MISR can also identify three to four distinct size groups between 0.1 and 2.0 microns characteristic radius, and two to three compositional groups over the natural range of indices of refraction.

These results indicate that MISR can distinguish about a dozen groupings of particles over the natural range of physical properties: 3 sizes, 2 or 3 compositions, and spherical vs. randomly oriented nonspherical particles. This represents a major improvement over current operational remote sensing aerosol retrievals, suggesting that with MISR data, we should be able to track air masses on a global scale based on the microphysical properties of the aerosols within them.

The generic retrieval produces aerosol physical properties with a minimum of assumptions; it is a good way to assess the information content of observations. But the effective column particle properties obtained may not correspond to any particles that are actually observed in the field or predicted by transport models. Under natural conditions, particle types are mixed. Constraints on the mixes of particles in the air mass are needed:

- to identify air mass source regions
- to track the evolution of air masses as they are advected downstream from their sources
- to make meaningful comparisons between MISR results and *in situ* aerosol samples
- to make meaningful comparisons between MISR retrievals and transport model results

In this paper, we explore the issue of distinguishing external mixtures of particle types. Since it is impractical to investigate the sensitivity of MISR to every conceivable mixture of every possible pure particle type, we adopt in the current paper a "climatological" retrieval approach. We explore how MISR can distinguish among assumed, climatologically likely, mixtures of pure particle types. The additional assumptions allow us to probe directly the way MISR might distinguish air masses containing common mixtures of aerosols in Earth's atmosphere, and to compare retrieval

results with *in situ* observations and with aerosol transport model predictions. The operational MISR aerosol retrieval, which will produce the first standard MISR aerosol products, is a form of climatological retrieval, using an efficient lookup table technique to match observations to a constrained set of aerosol mixtures [*Martonchik et al.*, 1998].

In the next section, we identify mixtures of particles we expect to find, based on an analysis of published global, monthly, aerosol transport model results and some measurements. We use these to set practical limits on the range of mixtures we consider in the sensitivity study. We also make an effort to assess the quality of the climatology data, since the value of a climatological retrieval rests on the quality of the assumed climatology. Section 3 describes the way we analyze the multi-dimensional particle mixture sensitivity data. As with the previous studies, we concentrate on situations under which the MISR sensitivity to particle properties (except possibly absorption) is likely to be greatest: over cloud-free, calm ocean. Results and conclusions are presented in the subsequent sections.

2. What Mixes of Particles Do We Expect to Find?

One of the motivations for flying MISR and other EOS instruments is that current knowledge of the global-scale distribution of aerosol types is inadequate for the purposes of many climate change studies. However, the slate is not completely blank, which is fortunate, since we could not examine every possible mixture of all particle types in a sensitivity study. We use results from a collection of global transport models [summarized by *Tegen et al.*, 1997] and other data to identify as small a set of aerosol mixtures as possible, that can represent the range of air mass types we expect to find in the atmosphere. The sensitivity study, presented in subsequent sections, will ask how well MISR data can distinguish the air mass types that appear in this simplified climatology.

Each transport model we use as input estimates the monthly global distribution of one or more of 6 common aerosol types: Sulfates, Carbonaceous, and Black Carbon particles [*Liousse et al.*, 1996], Accumulation and Coarse Mode Mineral Dust [*Tegen and Fung*, 1995], and Sea Salt particles [*Tegen et al.*, 1997]. Some characteristics of these models are given in Table 1. We resampled each model output to a uniform 1° x 1° global grid, using bilinear interpolation. (At the 1° scale, the model results are smooth, so resampling does not introduce spurious gradients.) We linearly superposed the 6 data planes to obtain a global grid containing monthly estimates of total column aerosol optical depth and fraction of total optical depth at mid-visible wavelengths (MISR Band 2, at 558 nm) contributed by each of the component aerosol types.

2.1. Mixture Classification

The goal of this subsection is to boil the transport model results down to a small number of representative air mass types, made from the 6 particle types, that describe the global-scale spatial and temporal aerosol mixture patterns at a level of detail appropriate to the MISR aerosol retrievals. We expect the MISR data to allow no more than about a dozen distinctions based on aerosol microphysical properties [*Kahn et al., 1998*]. To be useful for our purpose, we seek a similar number of representative air mass types in the simplified aerosol climatology. Our presentation of the aerosol climatology will also reflect the kinds of global-scale data products we expect to derive from MISR: monthly global maps of air mass type and aerosol total column optical depth.

The actual MISR aerosol algorithm adopts different retrieval strategies for observations taken over dark water, dense dark vegetation, and heterogeneous land [*Martonchik et al.*, 1998]. The amount of information about aerosol properties in the retrieval depends upon the contribution upwelling radiation from the surface makes to the MISR measurements, and on our ability to model that contribution. Until we receive data from MISR itself, all our assessments are based only on

theoretical simulations. We expect to obtain the tightest constraints on aerosol particle properties (except possibly aerosol single scattering albedo) for MISR observations taken over dark water (oceans and inland seas), and for aerosol optical depths between 0.1 and 1.0 [*Kahn et al., 1998*]. By contrast, confidence in the transport model aerosol types is not so strongly linked to surface properties.

We begin identifying the global patterns by defining mixing groups, based on the 4 particle types that contribute most to the total column optical depth (at about 558 nm wavelength) at each location and month in the aggregated transport model results. Plate 1(a-d) gives maps of particle mixing group for 4 months spanning the year. The corresponding total column optical depths, also derived from the aggregated transport model results, are given in Plate 3(a-d). Although the transport model results for most aerosol types were developed independent of each other, the mixture data are highly clustered. Of the 15 possible combinations of 4 particle types that can be made from the 6 types included in the climatology, only 5 combinations are needed to describe the top 4 components for nearly the entire data set. These 5 mixing groups are the major headings in Table 2.

All 5 mixing groups contain sulfate particles. We label as "Maritime" those groups that contain sea salt particles; we call "Continental" those groups that do not have sea salt among the 4 most abundant particle types, but do have accumulation mode dust particles. The other aerosol components contributing to each group determine whether the classification is "Dusty," "Carbonaceous," or "Black Carbon." Representative colors for the maps in Plate 1 and elsewhere were chosen so the most common Maritime classes appear in shades of blue, the most common Continental classes are brown. For those that remain, classes rich in Black Carbon are gray, those with much Carbonaceous aerosol are green, and ones abundant in Coarse Dust are yellow.

The actual proportions of the 4 components within each group are also highly clustered in the transport model results. We illustrate this in Plate 2, which shows slices through a 4-dimensional histogram of the aerosol components for the "Carbonaceous + Dusty Continental" mixing group, aggregated over the year. The full diagram is a tetrahedron, divided into voxels that correspond to mixtures having different proportions of each of the 4 component particle types (in this case: Sulfate, Accumulation Mode Dust, Coarse Mode Dust, and Carbonaceous particles). Each triangular facet of the tetrahedron is a standard ternary mixing diagram; the vertices represent 100% of a component, along the edges are mixtures of only 2 components, and in the facet interior are 3-component mixtures of systematically varying proportions. Interior points to the tetrahedron correspond to 4-component mixtures. For this histogram, we have chosen a 5% increment, so, for example, the voxel at one of the vertices of the tetrahedron is colored according to the number of occurrences in the climatology of a mixture with 95% to 100% of the end member associated with that vertex.

Shown in Plate 2 are 6 planes with constant Coarse Mode Dust fraction, corresponding to bins containing Coarse Mode Dust of (a) 25% to 30%, (b) 20% to 25%, (c) 15% to 20%, (d) 10% to 15%, (e) 5% to 10%, and (f) 0% to 5%, respectively. Red shades indicate high counts (>2500), gray are intermediate values (about 1200 to 2500), light blue are values between 600 and 1200, dark blue are counts below 600, and black are locations for which there were no mixtures in the climatology falling in that mixture bin. The maximum value is a bright red voxel in panel (e) with 5,895 counts, and an average mixture of 47% Sulfate, 13% Carbonaceous, 32% Accumulation Mode Dust, and 8% Coarse Mode Dust (percent by optical depth). In the computer-interactive tool, we can select 4-dimensional histograms for any mixing group, aggregated either by month or for the full year. We can view planes having constant fraction of any component, and click on individual voxels in the planar representations to bring up the number of counts and mean proportions of each component contributing to that voxel.

Of 1,771 voxels in this histogram, only 21% are non-zero. For this mixing group, planes with the Coarse Mode Dust component greater than 40% are all empty. The voxels with non-zero counts

are concentrated in a small part of the volume, and there are several local maxima, some of which show up better in the monthly histograms than in the annual aggregate. The other 4 mixing groups behave similarly, and contain between 11% and 34% non-zero voxels (Table 2), all concentrated in 2 or 3 clusters. That natural mixtures of aerosols are highly clustered in this way is no surprise to those who measure aerosol chemical properties in the field; field observers have identified distinct aerosol air mass types for decades [e.g., *Prospero et al., 1983, d'Almeida et al.*, 1991; and references therein]. It is reassuring that the aggregated transport models also produce clusters in aerosol mixture proportions. These observations suggest that it is possible to produce a vastly simplified aerosol climatology to summarize the global, monthly data in a manner appropriate to the MISR sensitivity study.

We used a K-means clustering algorithm [*Hartigan and Wong*, 1979] to locate the centroids of clusters in each mixing group. Given a number (K) of clusters to be identified, the alogrithm locates cluster centers that minimize the sum (over all points) of the squared distance from each point in the space to its nearest cluster center. (We use the percent contributions to total column optical depth of the 4 components as 4 linear metrics spanning the space.) K-means algorithms depend heavily on the choice of K, and also on initial guesses for the cluster center locations. We used an interactive, computer-based 4-dimensional histogram tool (Plate 2) to help identify initial guesses. We also experimented with the number and order of initialization values to assure that we found stable solutions, and reviewed the monthly histograms and maps to search for clusters that may not show up well in the annual aggregates. We selected resulting 13 cluster centroids, given in Table 2, are our representative aerosol air mass types. The spatial distributions of the mixing groups, sub-divided into the 13 air mass types, are shown for 4 months spanning the year in Plate 1(e-h). Some attributes of air mass type spatial and temporal behavior are also summarized under "Notes" in Table 2.

2.2. Assessment of the Simplified Climatology

Since the value of the climatological retrieval rests on the quality of the assumed climatology, we made an effort to understand its strengths and limitations. In qualitative terms, the patterns created by our classification scheme compare favorably with expectation and with observations [*Tegen et al., 1997 and* references therein; see also Husar et al., 1998]. Continental classes predominate over most land masses and downwind in some coastal regions; Maritime classes are found away from continents. Black Carbon classes appear over Europe, eastern China, and tropical Africa and South America, and Carbonaceous classes are found in the equatorial zone, persistently over Indonesia. Coarse dust is a major component over deserts and surrounding areas. Over oceans, more distant from the terrestrial sources of dust, biomass burning, or soot, the air masses tend to contain larger fractions of Sulfates and Sea Salt particles.

The classification is less meaningful where optical depth is low, since tiny amounts of one particle type can determine the class. This occurs in the polar regions, remote oceans, and high-latitude continental areas, particularly in winter. More generally, the climatology's optical depths, illustrated in Plate 3(a-d), also match qualitative, global-scale expectations: they are highest over well-known source regions such as the Sahara and Gobi deserts, the tropical rainforests and subtropical savannas during burning seasons, and major industrial areas such as eastern Europe and eastern China. Total column optical depths are also higher in summer than in winter in each hemisphere, and seasonal effects are greater in the land-rich northern hemisphere.

Our evaluation must take into account uncertainties in the transport models themselves, such as the assumption, for each particle type, of a universal value for the factor that converts column mass abundance to optical depth (Table 1). Due in part to the choices made for these factors, Maritime classes appear over western North America and parts of South America and subtropical Africa between January and April. Carbonaceous particles appear among the top 4 particle types at almost all locations and times. As discussed by Tegen et al.[1997], there are other limitations to the

transport model results, caused by model error, simplified parameterizations of physical processes, and unmodeled aspects of natural variability.

We take a few steps in the direction of a more quantitative, global assessment of the simplified climatology. We compare the model optical depth results with monthly aerosol optical depth retrievals over global oceans from the NOAA AVHRR measurements [Stowe et al., 1997; Rao et al., 1989; Table 1]. The AVHRR retrieval is not specific as to particle type. Aerosol indices of refraction are assumed to be globally constant and equal to 1.4 + 0.0 i.. Particles are taken to have a log-normal size distribution with effective radius rm = 0.1 microns and distribution width _ = 2.03. The ocean surface is assumed to have a reflectivity at 0.67 microns of 0.002. Retrievals are performed only over cloud-free ocean, between 70° north and 70° south latitude.

Global maps of the difference in total column aerosol optical depth between the AVHRR and transport model results, for 4 months in 1989, a year without major volcanic contributions to the global aerosol load, are shown in Plate 3(e-h). The comparison must be viewed with caution: the AVHRR data are skewed toward cloud-free regions, which may produce an underestimate of aerosol optical depths on regional scales [Tegen et al.,1997]); they are not sensitive to contributions from absorbing particles, and they are reported at 670 nm wavelength, which is expected to provide values about 10% lower than model results at 550 nm for the most common particle types [Stowe et al., 1997]. Nevertheless, the AVHRR data often report larger column optical depths than the aggregate of aerosol transport models; histograms of monthly global optical depth difference for 1° by 1° spatial cells (not shown) are skewed by about 0.05 in the direction of higher AVHRR values.

The AVHRR optical depth values range from the limit of detection up to about 1.0, and are generally within 0.2 of the model predictions. On a global scale, the biggest discrepancies between AVHRR and the models occur in the corridor where Sahara dust is advected westward across the Atlantic, and in the Arabian Sea. Optical depths are relatively high in these regions to begin with. The AVHRR values usually exceed those of the model results by 0.25 to 0.5 over the Atlantic (the extreme discrepancy is 0.8, and occurs in July), whereas the model results are mostly between 0.1 and 0.3 higher than AVHRR in the Arabian Sea, with the largest difference just under 0.5. For the purposes of the MISR sensitivity study, this represents good agreement; it provides us with climatological ranges of optical depth values upon which to focus the simulations.

To further assess the particle mixture classification part of the climatology, we reclassified the air masses after replacing the sulfate model from Liousse et al. [1996] with model results from Chin et al., [1996; see Table 1]. (Only for Sulfates were we able to obtain comparable, monthly global transport model results from several sources.) Although this is far from a thorough test, it is a useful step to take for this study, since we are interested in general characteristics rather than details. We view differences between the two classifications as suggestive of the accumulated uncertainties in the climatology as they relate to our simple classification.

Differences between the two sets of models resulted in different air mass classifications over Europe, and in some low optical depth regions of the North Atlantic and North Pacific. In particular, where sulfur emissions are high, such as Europe, the Liousse et al. [1996] model produces several times the optical depth in sulfate particles compared to Chin et al. The differences are most pronounced in summer.

With these exceptions, an instrument sensitive to the differences in aerosol mixtures captured by our classification scheme would identify similar aerosol air mass types everywhere else around the globe. Despite the qualitative nature of our classification scheme, its value for the MISR sensitivity study stems from the agreement with expectation, since the classification was made based only on relative abundances of particle types, and not on any externally imposed spatial or temporal constraints. Similarly, we hope to derive rather than assume the spatial and temporal patterns of aerosol mixture types from MISR data.

2.3. Assumed Component Particle Type Optical Properties

Using the transport model results, we obtained representative mixtures of 4 components from among 6 aerosol types, given in fractions of the total column optical depth at mid-visible wavelengths, on a monthly, 1° by 1° global grid. We also obtained representative values of total column optical depth on the same grid. To complete the climatology needed to assess MISR sensitivity, we must select optical properties for each of the 6 aerosol types. This is the most difficult part of the climatology to specify, since aerosol properties vary on many spatial and temporal scales. For example, hygroscopic particle properties change substantially depending on the relative humidity [e.g., *Hegg et al.*, 1993], and mineral dust properties vary with source region [*Sokolik and Toon*, 1996].

Since we expect MISR to distinguish about 3 size groupings, 2 shapes, and 2 colors under good observing conditions [*Kahn et al.*, 1998; 1997], we selected just one representative set of properties for each of the 6 aerosol types in this sensitivity study, except Sulfates. We hydrated the Sulfate particles to equilibrium at 70% relative humidity for "Continental" air mass types, and to 80% for "Maritime" air masses using the hydration model of *Hanel* [1976]. We also defined 2 vertical distributions for Accumulation Mode Mineral Dust; one, used for "Continental" air mass types, places all the dust in a near-surface layer, as we do for all other particle types. The second, used for "Maritime" air masses to simulate dust particles transported far from their source regions, distributes the particles between 5 and 10 km above the surface, with a scale height of 10 km. Our choices for particle properties are given in Table 3. They are abstracted from standard sources, as referenced in this table. We used a Mie algorithm to relate physical to optical properties for the spherical particles; for non-spherical Mineral Dust and cirrus, we obtained T-matrix results from *Mishchenko et al.* [1996; 1997; and personal communication]. Extinction and scattering properties for distributions of particles are calculated as weighted averages. The log-normal weighting function used is

$$lgnrm\,(r) = \frac{1}{r \ln(\sigma)\sqrt{2\pi}} \exp\left[-\frac{\left(\ln(r) - \ln(r_c)\right)^2}{2\left(\ln(\sigma)\right)^2}\right] \qquad (1)$$

The width parameter (σ) and characteristic radius (r_c) for each case is given in Table 3.

Of special interest is the last column in Table 3, which gives a "Particle Size/Shape Category" for each entry. These relate to the particle scattering phase functions shown in Figure 1. The scattering angles imaged by the 9 MISR cameras for a typical mid-latitude location are superposed in this figure. (At high latitudes, the range of scattering angles sampled by MISR extends from about 40° to 160°, whereas at low latitudes it is limited to between about 100° and 165°.)

The prototypical Black Carbon particle distribution produces a characteristic "small particle" scattering phase function. (For small sized particles, particle shape does not alter the scattering phase function, so the distinction between spherical and non-spherical is moot.) Accumulation Mode Mineral Dust is a medium, nonspherical particle type, producing a relatively flat scattering phase function between 70° and 160° scattering angle. Carbonaceous particles, as well as the two Sulfate particle types, are categorized as medium, spherical. The Coarse Mode Mineral Dust and Sea Salt are a large, non-spherical and large, spherical particle types, respectively. Each has a steeply sloped scattering phase function at small scattering angles. The thin cirrus model produces a scattering phase function that is distinct from all the other particle types. We also expect to distinguish absorbing ("dirty") from non-absorbing ("clean") particles. In Table 3, the Mineral Dust, Carbonaceous, and Black Carbon particles are absorbing. It is on the basis of these

differences among particle scattering phase functions and absorption characteristics that we expect to discriminate among natural mixes of particles with MISR data.

3. Our Approach to the Aerosol Mixture Sensitivity Study

Our approach to the climatological sensitivity study is similar to that adopted by *Kahn et al.* [1998] for the generic retrieval study. Prior to launch of the MISR instrument, we rely on simulations of top-of-atmosphere radiation to explore the sensitivity of multi-angle observations to aerosol properties. The MISR Team has developed a radiative transfer code, based on the adding-doubling method [*Hansen and Travis*, 1974]. It simulates reflectances as would be observed by MISR for arbitrary choice of aerosol mixture, amount, and vertical distribution, variable surface reflectance properties, and user-selected sun and viewing geometry [*Diner et al.*, 1998]. Radiances for mixtures of aerosol types are obtained by combining radiances for the individual components, weighted by fractional contribution to optical depth, according to the modified linear mixing method of *Abdou et al.* [1997]. For the present study we simulated MISR measurements over a Fresnel-reflecting flat ocean surface, in a cloud-free, Rayleigh scattering atmosphere with a surface pressure of 1.013 bar, a standard mid-latitude temperature profile, and aerosols concentrated in a near-surface layer.

We assume here that the vertical distribution of aerosols has a negligible effect on the results. Our tests with particles inside and above the Rayleigh scattering layer show that particularly at the blue and green wavelengths, and at the steepest emission angles, the effect may be significant. But most atmospheric aerosols are concentrated near the surface, and the MISR dark water retrievals use only the red and infrared channels, for which Rayleigh scattering is small. In the actual MISR retrievals we will consider at least a "transported mineral dust" particle type, that models desert dust advected high in the atmosphere; other particle models will be added as needed when we are analyzing MISR data and associated field measurements. In MISR retrievals over ocean, we will also model sun glint and whitecaps, which depend on near-surface wind speed [*Martonchik et al.*, 1998]. And of course, we anticipate modifying the MISR retrieval algorithm, as needed, once we have experience working with spacecraft data.

We designate one set of simulated reflectances as the MISR "measurements." For a measurement, the atmosphere has a fixed total aerosol optical depth (τ_a) and specified fractional contributions from each of 4 component particle types. We then test whether the measured radiances can be distinguished, within instrument uncertainty, from a series of "comparison" model reflectances. The 5 mixing groups identified in the climatology and listed as the major headings in Table 2 define the space of comparison models. Each comparison model represents a choice of 4 component particle types. We vary the fractional optical depth contributions of each of the component particle types systematically from 0 to 100%.

Tests results for a set of measurements against all possible comparison models within a mixing group can be arranged in a tetrahedron, similar to the 4-dimensional histograms used for the climatology analysis (Plate 2). The vertices of the tetrahedron represent tests against comparison models containing 100% of each of the 4 components, the edges are tests against mixtures of 2 components, the facets show tests against 3 components arrayed as in standard ternary diagrams, and the interior voxels represent test against 4-component mixtures. We use a grid of 5% steps in each dimension.

We also vary the total aerosol optical depth (τ_c) for comparison models over a grid, ranging from 0 to 1 in steps of 0.05. So the entire comparison-model parameter space for a climatological retrieval consists of 5 mixing groups, each composed of 21 tetrahedra that cover the range of total optical depth values. The goal of this sensitivity study is to determine the ranges of comparison model

particle mixtures and total optical depths that give acceptable matches to the 13 climatologically representative atmospheric air mass types listed in Table 2.

3.1. Testing Agreement Between "Measurements" and Comparison Models

Over ocean, the MISR retrieval makes use of up to 18 measurements: 9 angles at each of the 2 longest MISR wavelengths (Bands 3 and 4, centered at 672 and 866 nm, respectively), where the water surface is darkest. We define 4 test variables to decide whether a comparison model is consistent with the measurements. Each is based on the χ^2 statistical formalism [e.g., *Bevington and Robinson*, 1992].

One test variable weights the contributions from each observed reflectance according to the slant path through the atmosphere of the observation:

$$\chi^2_{abs} = \frac{1}{N\langle w_k \rangle} \sum_{l=3}^{4} \sum_{k=1}^{9} \frac{w_k \left[\rho_{meas}(l,k) - \rho_{comp}(l,k) \right]^2}{\sigma^2_{abs}(l,k)} \qquad (2)$$

where ρ_{meas} is the simulated "measurement" of atmospheric equivalent reflectance and ρ_{comp} is the simulated equivalent reflectance for the comparison model. (We define equivalent reflectance as the radiance multiplied by π, and divided by the exo-atmospheric solar irradiance at normal incidence.) l and k are the indices for wavelength band and camera, N is the number of measurements included in the calculation, w_k are weights, chosen to be the inverse of the cosine of the emission angle appropriate to each camera k, $\langle w_k \rangle$ is the average of weights for all the measurements included in the summation. σ_{abs} $(l,k;\ \rho_{meas})$ is the absolute calibration uncertainty in the equivalent reflectance for MISR band l and camera k.. For MISR, the nominal value of σ_{abs} falls between 0.03 for a target with equivalent reflectance of 100%, and 0.06 for an equivalent reflectance of 5%, in all channels [*Diner et al.*, 1998]. For the simulations, we model σ_{abs} as varying linearly with equivalent reflectance.

χ^2_{abs} alone reduces 18 measurements to a single statistic. χ^2_{abs} emphasizes the absolute reflectance, which depends heavily on aerosol optical depth for bright aerosols over a dark surface. However, there is more information in the measurements that we can use to improve the retrieval discrimination ability.

A second χ^2 test variable emphasizes the geometric properties of the scattering, which depend heavily on particle size and shape. The camera-to-camera relative uncertainty is small compared to the absolute uncertainty. The χ^2_{geom} test variable takes advantage of this fact -- each spectral measurement is divided by the corresponding spectral measurement in the nadir camera:

$$\chi^2_{geom} = \frac{1}{N\langle w_k \rangle} \sum_{l=3}^{4} \sum_{\substack{k=1 \\ k \neq nadir}}^{9} \frac{w_k \left[\dfrac{\rho_{meas}(l,k)}{\rho_{meas}(l,nadir)} - \dfrac{\rho_{comp}(l,k)}{\rho_{comp}(l,nadir)} \right]^2}{\sigma^2_{geom}(l,k)} \qquad (3a)$$

Here σ^2_{geom} (a dimensionless quantity) is the uncertainty in the camera-to-camera equivalent reflectance ratio, derived from the expansion of errors for a ratio of measurements ($\sigma^2(f(x,y)) = (df/dx)^2 \sigma_x^2 + (df/dy)^2 \sigma_y^2$ [e.g., *Bevington and Robinson*, 1992]):

$$\sigma^2_{geom}(l,k) = \frac{\sigma^2_{cam}(l,k)}{\rho^2_{meas}(l,nadir)} + \frac{\sigma^2_{cam}(l,nadir)\ \rho^2_{meas}(l,k)}{\rho^4_{meas}(l,nadir)} \qquad (3b)$$

$\sigma_{cam}(l,k)$ is the contribution of (band l, camera k) to the camera-to-camera relative calibration reflectance uncertainty. σ_{cam} is nominally one third the corresponding value of σ_{abs} for the MISR instrument [*Diner et al.*, 1998]. Note that σ_{cam} includes the effects of systematic calibration errors for ratios of equivalent reflectance between cameras, as well as random error due to instrument noise, though the latter has been neglected in these simulations, based on the high signal-to-noise ratio demonstrated during MISR camera testing [*Bruegge et al.*, 1998].

Similarly, we define a spectral χ^2 as:

$$\chi^2_{spec} = \frac{1}{N < w_k >} \sum_{k=1}^{9} \frac{w_k \left[\frac{\rho_{meas}(band\ 4,k)}{\rho_{meas}(band\ 3,k)} - \frac{\rho_{comp}(band\ 4,k)}{\rho_{comp}(band\ 3,k)} \right]^2}{\sigma^2_{spec}(l,k)} \qquad (4a)$$

with:

$$\sigma^2_{spec}(l,k) = \frac{\sigma^2_{band}(l,k)}{\rho^2_{meas}(band\ 3,\ k)} + \frac{\sigma^2_{band}(band\ 3,k)\ \rho^2_{meas}(l,k)}{\rho^4_{meas}(band\ 3,\ k)} \qquad (4b)$$

$\sigma_{band}(l,k)$ is the contribution of (band l, camera k) to the band-to-band relative calibration reflectance uncertainty. σ_{band} is nominally one third the corresponding value of σ_{abs} for the MISR instrument.

We include a maximum deviation test variable that is the single largest term contributing to χ^2_{abs} (see equation (2)):

$$\chi^2_{\max dev} = \underset{l,k}{Max} \frac{\left[\rho_{meas}(l,k) - \rho_{comp}(l,k) \right]^2}{\sigma^2_{abs}(l,k)} \qquad (5)$$

All the other test variables are averages of up to 18 measurements. χ^2_{maxdev} makes greatest use of any band-specific or scattering-angle-specific phenomenon, such as a rainbow or a spectral absorption feature, in discriminating between the measurements and comparison models.

3.2. Evaluating the χ^2 Test Variables

We defined 4 dependent variables to be used in comparing the measurements with the models (χ^2_{abs}, χ^2_{geom}, χ^2_{spec}, and χ^2_{maxdev}). Since each χ^2 variable is normalized to the number of channels used, they are "reduced" χ^2 quantities, and a value less than or about unity implies that the comparison model is indistinguishable from the measurements. Values larger than about 1 imply that the comparison model is not likely to be consistent with the observations. In more detail, $\chi^2 <$ 1 means that the average difference between the measured and comparison quantities is less than the associated measurement error. If the quantity in the numerator of a reduced χ^2 variable definition with 17 degrees of freedom is sampled from a population of random variables, an upper bound of 1 corresponds formally to an average confidence of about 50% that we are not rejecting a comparison model when in fact it should be accepted; for an upper bound of 2, that confidence increases to almost 99% [*Bevington and Robinson*, 1992]. This is not strictly true for the "χ^2" variables defined here. They are actually the averages of correlated measurements from multiple bands and cameras, so a given upper bound is likely to be a less stringent constraint. Each term contributing to these variables may itself be distributed as χ^2.

To illustrate the values of the test variables, we developed a color bar with 3 segments: a logarithmic segment for values between 10^{-5} and 1 depicted in shades of blue, a logarithmic segment for values between 5 and 10^4 depicted in shades of red, and a linear segment shown in light green, yellow, and orange shades for the intermediate values [*Kahn et al.*, 1998]. Thus, red shades in the figures indicate situations where the model is clearly distinguishable from the measurement, whereas blue shades indicate that the model is indistinguishable from the measurement. Black is reserved for exact agreement between model and measurement, which can occur in this study because we are working with simulated observations. Note that the color table has been designed so that if these figures are photocopied in black and white, first-order information about the ability to distinguish among models is preserved.

4. Sensitivity to Natural Aerosol Mixes

We are now ready to assess MISR's ability to retrieve climatologically likely aerosol mixtures over dark water. We begin with simulations that test the sensitivity of MISR to each of the 13 representative Air Mass Types identified in Section 2.1 and listed in Table 2. Table 2 also defines the 5 Mixing Groups that cover every proportion of mixture for the climatologically likely combinations of 6 pure particle types. The sensitivity study is accomplished by identifying the ranges of mixtures within all 5 Mixing Groups that give satisfactory matches to each of the 13 representative Air Mass Types. A narrow range indicates that MISR retrievals should be good at identifying that Air Mass Type. Once the general patterns for all 13 air mass types have been characterized and explained in terms of the physical properties of the component particles, we consider the possible effects of thin cirrus upon the results.

4.1. MISR Sensitivity to 13 Representative Air Mass Types, Based on 5 Climatologically Likely Mixing Groups

We begin this section by taking a close look at several specific cases, and then examine summaries of the entire comparison space. Plate 4 is shows the results of tests between simulated MISR measurements for an atmosphere with aerosol Air Mass Type 2a (Table 2), and the 1771 comparison model mixtures that comprise Mixing Group 2 (Dusty Maritime + Coarse Dust, Table 2). The optical depth in MISR Band 2 is set to 0.5 for both atmosphere and the comparison models this figure, and typical MISR mid-latitude geometry has been adopted. The comparison model cases are arranged in a tetrahedron, and Plate 4 shows slices through this tetrahedron that cover the interesting part of the space. Each pixel is divided into 5 fields. The upper left sub-pixel

is colored with the result of the χ^2_{abs} test, the upper right has the result of the χ^2_{geom} test, the lower left shows the $\chi^2_{max\ dev}$ test, and the lower right contains the χ^2_{spec} test, each using the color bar described in Section 3.2. The background is colored with the result of the most constraining of these 4 tests (the one with the highest value), since, if any one of the tests indicates that the comparison model does not match the observation, the comparison model must be rejected. We call this value χ^2_{max}.

Only 4 planes in Plate 4 have pixels with $\chi^2_{max} < 1$. So if we use this as the criterion for accepting a comparison model, the Coarse Mineral Dust optical depth fraction is constrained to fall between 5% and 20%, since no models with Coarse Mineral Dust fraction outside this range match the observations. Similarly, the Sulfate Particle optical depth fraction is confined to the range 50% to 55%, Accumulation Mode Mineral Dust must fall between 5% and 35% and Sea Salt is constrained between 5% and 25%. Plate 4 also indicates the correlations among acceptable fractions for each component. The actual composition for Air Mass Type 2a is: 10% Coarse Mode Mineral Dust, 52% Sulfate, 21% Accumulation Mode Mineral Dust, and 17% Sea Salt. In this case, the MISR retrieval constrains all the component particle types in the mixture to within 20% of the true value, and the best constraint is better than 5%.

Plate 5 (a-d) shows sections through the tetrahedral comparison space for Mixing Group 4 (Carbonaceous + Dusty Continental), for an atmosphere with aerosol composition given by Air Mass Type 4a (Table 2). Four planes with constant Coarse Mode Dust fraction ranging from 0% to 15% are presented. In this case, the $\chi^2_{max} < 1$ criterion yields solutions only for Coarse Mode Mineral Dust between 0% and 10% optical depth contribution in MISR Band 2, and for Accumulation Mode Mineral Dust between 20% and 25%. The Sulfate and Carbonaceous particles form a mixing line; models with as much as 70% Sulfate (and 0% Carbonaceous particles) or as little as 40% Sulfate (and 40% Carbonaceous particles) meet the acceptance criterion. For these mixtures of particles over a dark water surface, a simulated MISR retrieval using the red and near-infrared bands and all 9 angles can not distinguish Sulfates, which are "medium, spherical, non-absorbing" particles, from Carbonaceous, which are "medium, spherical, absorbing" particles (Table 3). However, the sum of the fractional contributions of Sulfate and Carbonaceous particles to optical depth is always around 75%. This is close to the true value, the sum of 61% Sulfate and 13% Carbonaceous particle fractional optical depths.

A similar result appears in Plate 5 (e-h), which examines the sensitivity of MISR to an atmosphere having aerosol composition given by Air Mass Type 4c, in the tetrahedral comparison space for Mixing Group 4. Air Mass Type 4c contains only 22% Sulfate and an 11% Carbonaceous particle optical depth contributions, along with 51% Accumulation Mode Mineral Dust, and 16% Coarse Mode Mineral Dust. With the $\chi^2_{max} < 1$ criterion, acceptable matches are found for Coarse Mode Dust between 10% and 20%, and Accumulation Mode Dust from 45% to 55%, reflecting the larger dust contribution for Air Mass Type 4c than for 4a. Again, sensitivities are in the range of 10% to 20% around the expected value, except for Sulfate and Carbonaceous aerosols, which form a mixing line.

Figure 2 gives a more extensive though less detailed picture of MISR sensitivity to all 13 Representative Air Mass Types, as compared with every combination on 5% tetrahedral grids for all 5 Mixing Groups. There are 13 columns of whisker plots, one for each Representative Air Mass Type in Table 2. The first 5 rows are comparisons of the Air Mass Types with each of the 5 Mixing Groups. The horizontal axis for each whisker plot allows 6 positions, for each of the 6 pure particle types in this study. The vertical axis shows the range of fractional optical depth from 0 to 1. There are no more than 4 whiskers in each plot, corresponding to the components of the relevant Mixing Group. Each whisker indicates the largest and smallest fractional optical depth of that pure particle type, for any comparison model in the Mixing Group that meets the criterion χ^2_{max}

< 1. Longer whiskers indicate that acceptable comparison models span a wider range of fractional optical depth. Note that correlations among particle types, such are the relationship between Sulfate and Carbonaceous particles illustrated in Plate 5, are not shown in Figure 2. However, an "x" on each whisker indicates the component fractional optical depth for the comparison model in the relevant Mixing Group with the lowest value of χ^2_{max}. The last row of plots shows with "+" signs the actual fractions of pure particles contributing to the Air Mass Type for each column.

For Figure 2, the total atmospheric column optical depth, and that of all comparison models, is set to 0.5, and typical MISR mid-latitude geometry is used. Scanning down the columns, there are no matches at all for any of the 7 "Maritime" air masses in the "Continental" Mixing Groups (Groups 4 and 5). Sea Salt particles (large, spherical; Table 3) are distinctive to MISR when the background is dark water. Similarly, there is only one match for any "Continental" air mass in the 3 "Maritime" Mixing Groups. This match is for Air Mass 4b in Mixing Group 1. The acceptable comparison model has 40% Accumulation Mode Dust, similar to the Air Mass value, a combination of Sulfate and Carbonaceous particles that apparently accounts for the medium, spherical particles in the Air Mass, and none of the distinctive Sea Salt available in the Mixing Group but absent from the Air Mass. The χ^2_{max} for this model is 0.958.

Further examination of Figure 2 reveals that sensitivities to all components are within 10% to 20% or better of the expected value, except for the redundancy between Sulfates and Carbonaceous particles. The distinction between spherical and non-spherical particles is strong enough that there are no matches for Air Masses 2a and 2b, which contain Accumulation and Coarse Mode Dust, in Mixing Group 3, that lacks both these particle types. Continental Air Mass Types produce very similar ranges of Sulfates, Accumulation Mode Dust, and Carbonaceous particles in both Continental Mixing Groups. However, the retrievals find acceptable matches with either Black Carbon (small, absorbing) or Coarse Mode Dust (large, non-spherical, absorbing), when given atmospheres containing aerosols from the Continental Air Masses in our climatology. These Air Masses contain 20% or less of Black Carbon or Coarse Mode Dust particle types, the apparent limit on MISR sensitivity to particle properties in climatologically likely mixtures, for the dark water, 2-spectral-band retrieval situations simulated here.

We complete this section by varying the atmosphere and comparison model optical depths. From the generic sensitivity study [*Kahn et al., 1998*], we know that sensitivity decreases with decreasing atmospheric total column optical depth. Following the results of that paper, we also anticipate that regardless of composition, comparison models differing in total column optical depth by 20% or more should not match the atmosphere. There is a difference, however, between the generic and climatological retrievals. The generic retrieval involves only one set of effective, column-weighted particle phase function and indices of refraction for each atmosphere and each comparison model. The climatological retrieval is free to mix properties of up to 4 pure particle types, and occasionally the individual particle phase functions combine to produce spurious matches with larger optical depth differences. Fortunately, these tend to be isolated solutions, whereas there is usually a range of acceptable models surrounding the values for a correct solution, as shown in Figure 2. We illustrate and further examine spurious solutions below.

When the 13 atmospheres have optical depth 0.5, there are no matches for comparison models with optical depths less than 0.4, for any Mixing Group. Nor are there any matches for comparison models with optical depths greater than 0.65, except for Air Mass 5b in Mixing Group 3. Figure 3 is the whisker plot matrix for a mid-latitude case with atmospheric (Air Mass) total column aerosol optical depths set to 0.5 in MISR Band 2, and comparison model (Mixing Group) optical depths of 0.65.

In Figure 3, the match for Air Mass 5b in Mixing Group 3 involves 25% Black Carbon in the comparison model substituting for the combination of 12% Accumulation Mode Dust plus 9% Black Carbon in the Air Mass. A match for a single case of this Air Mass-Mixing Group

combination appear in whisker plot matrices with comparison model optical depths up to 0.75, although there are no matches anywhere else on the whisker plot matrices for these cases. As comparison model optical depth increases, the fractions of Black Carbon and Sulfate for the matching comparison model increase at the expense of the fraction of Carbonaceous particles.

The phase function plots for individual particle types in Figure 1, coupled with tetrahedral comparison matrix sections and detailed plots of camera-by-camera single scattering and total radiance (not shown), provide some insight into these matches. As optical depth for the comparison model increases, adding a larger fraction of Black Carbon helps bring the overall reflectance down (χ^2_{abs} is most sensitive to this). The Black Carbon phase function is relatively flat over the range of scattering angles viewed by the forward cameras (about 60° to 100°) and aft cameras (about 150° to 160°, see Figure 1). Since the phase function for Accumulation Mode Dust, which is in the atmosphere but absent from the comparison models, is also fairly flat over these angles, matches are possible. Sea Salt, which is in the comparison models but not the atmosphere, occurs at the 5% level for all matches. The phase function for this particle type is distinct in having relatively small values over the aft camera scattering angles, but high values in the forward camera range, which may compensate for the difference in curvature between the Accumulation Mode Dust and other particle types. The trade-off between Sulfate and Carbonaceous particles, present in both the atmosphere and comparison models, is apparently able to make up for the remaining differences.

The match in Figure 3 between Air Mass 5b in Mixing Group 5 is similar to the Group 3 case; increased Black Carbon fraction substitutes for Accumulation Mode Dust and keeps the absolute reflectance low, while small adjustments in Sulfates and Carbonaceous fractions complete the match. The remaining matches in Figure 3 involve Air Masses 1a, 1b, and 1c in Mixing Group 3. This again involves Black Carbon, which is in the comparison models but not in the atmospheres, and Accumulation Mode Dust, which is in the atmospheres but not the comparison models. Solutions again appear for relatively large fractions of Black Carbon, with Carbonaceous particles compensating for the remaining differences.

Since multiple scattering accounts for between 50% and 70% of the signal in all these cases, there are limits as to how far it is useful to carry these interpretations. We conclude that we can account qualitatively for the trends in these spurious matches. If this were a retrieval involving real data, such a match would be suspect because (1) only a few isolated cases give matches for each comparison model optical depth, rather than 5% to 20% ranges of fractional amounts, and (2) the amount of Black Carbon falls outside the climatologically likely range. The situation is far simpler for atmospheres with total column optical depth 0.5 and comparison models having lower optical depths. There is no particle in the climatology with a relatively flat scattering phase function that can increase reflectances, as Black Carbon lowers them when the comparison model optical depth is higher. For comparison models with optical depth below 0.4, there are no matches at all.

Figure 4, the whisker plot matrix for a mid-latitude case with atmospheric total column aerosol optical depths of 0.2 in MISR Band 2, and comparison model optical depths of 0.2, shows the degree to which information about particle properties decreases for lower atmospheric aerosol optical depth. (Though not illustrated, the retrieval sensitivity for atmospheres with column optical depth 0.1 is nearly the same as the 0.2 case.) As the retrievals become less specific, the number of matches in the whisker plot matrix grows. Solutions are found in Mixing Group 2 (which is Maritime) for all 6 Continental Air Mass Types, though the amount of Sea Salt in the solutions is always either 0% or 5%.

Solutions are found in Figure 4 for Sulfate-rich Continental Air Mass 4a in Mixing Group 1, though they contain no Sea Salt, and use a combination of Accumulation Mode Dust and Carbonaceous particles to account for the contributions of Coarse Dust in the atmosphere. There are also matches for Maritime Air Mass 1b in Mixing Groups 4 and 5. They require only 3 particle

types; the atmospheric Sea Salt is substituted with up to 10% additional Carbonaceous particles and a 5% to 20% decrease in Sulfates. Generally, in Figure 4, the whiskers are longer, and some of the substitutions occur more readily than in Figure 2. But the ability to distinguish large, spherical particles (Sea Salt), non-spherical particles (Accumulation and Coarse Mode Dust), and small, dark particles (Black Carbon) is preserved, at least within 20% of the expected values.

Looking at comparisons between atmospheres having 0.2 total column optical depth and models with different optical depths, there are no matches at all when the comparison model optical depths are 0.15 or lower, or when they are higher than 0.35. As with the more optically thicker atmospheres, spurious matches can occur when comparisons are made with models having higher optical depth and containing Black Carbon (Mixing Groups 3 and 5). This is shown in Figure 5. In all these cases, when the comparison model optical depth is 0.3 (or higher), Black Carbon accounts for 30% or more of the total optical depth, a climatologically high value that would be suspect in an actual retrieval.

4.2. MISR Sensitivity to Air Masses Containing Thin Cirrus

We expect to find optically thin hazes of cirrus ice crystals in the atmosphere at low latitudes, derived from deep convective systems, in mid latitudes, primarily as residuals of storm development, and at high latitudes as a consequence of storms and of low-temperature nucleation processes. The MISR data processing algorithms use several cloud detection approaches to eliminate observations containing clouds [e.g., *Diner et al.,* 1998a]. These include a view-angle and spectral-band-specific threshold technique, stereo matching to determine the heights of discrete scene features, and assessing the changes in spectral differences as a function of view angle to reveal high clouds. We also plan to use the cirrus product derived from the 1.38 micron channel on the nadir-viewing Moderate Resolution Imaging Spectrometer (MODIS) instrument [*Gao et al.,* 1993], that will fly on the same spacecraft as MISR. Although we expect these masks to be effective over a wide range of natural conditions, they are unlikely to be reliable when the cirrus normal optical depth is less than a few tenths at mid-visible wavelengths. So we are forced to consider thin cirrus in our climatological aerosol retrievals.

Fortunately, the optical properties of thin cirrus may be easier to model than those for thicker clouds. In particular, thin cirrus tends to have small (tens of microns), randomly oriented, fairly mono-disperse crystals [e.g., *Minnis et al.,* 1993]. For thicker cirrus, each of these simplifying characteristics is unlikely to be valid, and an admixture of liquid water droplets may also be present, even at very low temperatures [*Sassen et al.*, 1989]. For thin cirrus particle microphysical properties, we assume the fractal model results of *Mishchenko et al.* [1996]. They are included in Table 3 and Figure 1.

We have no specific climatological constraints on aerosol mixtures that include thin cirrus, a situation fundamentally different from that for the mixtures treated in the previous section. We must therefore ask a general question: How might the presence of cirrus ice particles, in optical depths up to a few tenths at mid-visible wavelengths, affect aerosol climatological retrieval results?

To this end we introduce 6 additional mixing groups, listed as the major headings in Table 4. Each group has cirrus particles and Sulfate components. As in Table 2, there are Maritime mixtures containing Sea Salt particles, and Continental groups that include Accumulation Mode Mineral Dust. One of the remaining aerosol types from Table 1 is chosen as the fourth component for each mixing group. We also selected 27 new Air Mass Types containing cirrus: 9 basic types, each subdivided into cases having 10%, 20% and 50% cirrus contributions to the total column aerosol optical depth.

We perform 3 additional sets of tests: atmospheres containing cirrus against comparison models without cirrus, atmospheres without cirrus against comparison models containing cirrus, and

atmospheres containing cirrus against comparison models containing cirrus. Since most of the behavior follows patterns described in Section 4.1, we provide only a brief overview of results.

Tests between atmospheres containing cirrus (Table 4) and comparison models without cirrus (Table 2) address the question: If the atmosphere contains thin cirrus, and we perform aerosol retrievals assuming a climatology that does not contain cirrus, how will the retrievals perform?

We begin with cases where half the mid-visible optical depth is contributed by cirrus. When the comparison model optical depths exceed those of the atmosphere by 10% or more, solutions appear only for models containing climatologically unlikely fractions of Black Carbon, regardless of whether the atmospheric optical depth is 0.5, 0.2, or 0.1. Cirrus particles are bright, and as with the non-cirrus atmospheres, Black Carbon can sometimes offset high optical depth, producing a comparison model that meets the acceptance criterion. Such results would be suspect, especially when the Black Carbon contribution is 20% or more. For atmospheres having 0.1, 0.2, and 0.5 aerosol optical depth, no solutions at all are found for comparison models with optical depths lower than 0.1, 0.15, and 0.40, respectively, on our grid of aerosol optical depths from 0.0 to 1.0 in 0.05 increments.

The situation is more complicated if the atmosphere and comparison model optical depths nearly match. When the atmospheric optical depth is 0.5 and comparison model optical depths are between 0.40 and 0.55, spurious solutions occur for Maritime Air Masses containing cirrus in Continental Mixing Groups that do not (Figure 6). In these cases, Accumulation and sometimes Coarse Mode Dust account for part of the atmospheric cirrus contribution, and the rest is attributed by the retrieval to the Sulfate-Carbonaceous particle mix.

The spurious solutions rely on having just the right combination of cirrus and Sea Salt in the atmosphere. If the atmosphere contains too much Sea Salt (Air Mass C1b.5 in Figure 6), comparison models can not be found to match the observed radiances. Referring to Figure 1, Sea Salt scatters a large fraction of incident light into scattering angles between 120° to 170° relative to the fraction scattered in the range 60° to 90°, as compared to other particle types. Cirrus produces the opposite trend. As a result, all combinations of the other available particle types produce radiance vs. scattering angle curves that are not flat enough to match the simulated observations, even with 50% cirrus to counter the behavior of Sea Salt (Figure 7). Conversely, if the atmosphere has 50% cirrus and no Sea Salt (all the cases on the right side of Figure 6), no comparison model formed from the remaining particle types can produce as steep a curve of radiance vs. scattering angle as the simulated observations. And having Sea Salt in the comparison space (top half of Figure 6) doesn't produce solutions either, because this only increases the differences in curvature between the radiance vs. scattering angle plots for the comparison models and the cirrus-rich atmospheres. For nearly all these cases, χ^2_{geom} is the largest of the 4 χ values.

We look next at cases where cirrus contributes only 10% or 20% to the total aerosol optical depth and there is no cirrus in the comparison model spaces. Again matches for comparison models with optical depths higher than those of the atmosphere involve climatologically large fractions of either Black Carbon, or in a few cases, Coarse Mode Dust. And solutions for comparison models with optical depths lower than those of the atmosphere are again rare. For comparison models with total column optical depths near that of the atmosphere, increased Accumulation and/or Coarse Mode Dust, along with a larger fraction of Sulfate-Carbonaceous particles relative to the atmosphere, account for the spurious solutions that appear. However, with only 10% or 20% cirrus in the atmosphere, the retrieved mixtures for these cases are as close to the atmospheric composition as would be expected based on the results of Section 4.1. In an actual retrieval, the differences could not be distinguished from uncertainties in other factors, such as the assumed climatology.

In summary, if the atmosphere contains 10% or more thin cirrus, few comparison models that do not contain this particle type meet the retrieval acceptance criterion for any of the assumed

atmospheres. We can explain qualitatively the spurious matches that occur since we know the microphysical properties of the particles involved. For 10% or 20% cirrus fraction, the spurious results that appear still fall within the range of expected uncertainties that arise from other assumptions. In retrievals with MISR data, we would probably exclude those spurious solutions containing large fractions of Black Carbon or Coarse Mode Dust, based on climatological likelihood. Eliminating the few remaining cases (e.g., Figure 6), if they arose in an actual retrieval, would require information from other sources, or additional assumptions.

We address next the question: If the atmosphere does not contain cirrus, and we nevertheless perform aerosol retrievals assuming a climatology that does contain cirrus, how will the retrievals perform?

For cirrus-free atmospheres containing 0.1, 0.2, and 0.5 total aerosol optical depth, no solutions at all are found for cirrus-containing comparison models having optical depths lower than 0.1, 0.2, and 0.4, respectively, on our 0.05 optical depth grid. And paralleling earlier results, every match to the cirrus-free atmospheres by cirrus-containing comparison models having optical depth higher than 0.1, 0.2, and 0.55, respectively, involves considerable fractions of either Black Carbon or Coarse Mode Dust.

Nearly all the successful comparison models have column aerosol optical depth within 10% of the atmospheric aerosol optical depth value. Most solutions are 3-component matches to 4-component atmospheres, containing no cirrus, and either substituting Sulfate for all the Carbonaceous particles, or accommodating a small percentage of Black Carbon or Coarse Dust in the atmosphere by adjusting the comparison model's fractions of other particle types. There are also a few cases analogous to those in Figure 6. This time, the cirrus and Sea Salt are in comparison models that match cirrus-free, but usually dust-rich, Air Masses. As before, additional information would be needed to eliminate such spurious results if they occurred in an actual MISR retrieval.

There is one final question to ask in this section: How sensitive are the MISR retrievals to cirrus when it appears in the atmosphere and is included in the comparison models?

We have included cirrus in a way that introduces an additional degree of freedom into the problem. This does not reduce the ability of the 9-angle, 2-channel MISR dark water retrieval to constrain total aerosol optical depth, but it weakens the constraints that can be placed on the composition of aerosol mixtures. Figure 8 shows the situation when 20% of the atmospheric aerosol optical depth in MISR Band 2 is due to cirrus, and the total column aerosol optical depth (including cirrus) is 0.5. Scanning down the columns, atmospheres containing 20% or more Sea Salt or Accumulation Mode Dust are not matched by comparison models lacking Sea Salt or Dust, respectively. But other distinguishing behavior is difficult to find; there are multiple combinations of Sulfate, Carbonaceous, Accumulation Mode Dust, and cirrus that produce spurious solutions. Field measurements will be required to make many distinctions among aerosol Air Masses Types when the column also contains a significant fraction of cirrus.

5. Conclusions

In earlier theoretical work, we performed generic retrieval simulations for an instrument like MISR. Such retrievals make a minimum of assumptions about the particles present, and seek the cross-section-mean-weighted column aerosol properties. The results provide insight into the information content of the observations. We found that for natural ranges of particle properties, under good observing conditions, MISR can make about a dozen distinctions based on particle size (small, medium, large), shape (spherical and randomly oriented non-spherical), and composition (absorbing and non-absorbing), along with estimates of aerosol column optical depth [*Kahn et al.*, 1997; 1998].

A limitation of the generic retrieval approach is that cross-section-mean-weighted aerosol properties are difficult to compare with *in situ* field measurements, and with the results of any physically based aerosol transport model, since these describe the behavior of mixtures of individual particle types. The current paper explores climatological retrievals for simulated MISR data. Such retrievals constrain the proportions of individual particle types in climatologically likely mixtures. We conclude that multi-angle, multi-spectral imaging contains enough information to warrant adopting this retrieval approach as well.

Since the value of a climatological retrieval depends on the quality of an assumed climatology, we based our assumptions on results from some of the best available global monthly aerosol transport models. Our analysis shows that the entire global, monthly data set, aggregated from transport models for the 6 most common particle types, can be represented by a climatology containing only 5 Mixing Groups, each composed of all possible proportions of 4 externally mixed pure particle types. We also find that within each Mixing Group, the climatologically likely mixtures cluster into only 2 or 3 Air Mass Types having specific proportions of the 4 pure particle end-members. So we represent the range of climatologically likely aerosol mixtures with about 13 Representative Air Mass Types. These results are summarized in Table 2 and Plate 1.

To test MISR's sensitivity to aerosol mixtures, we adopt some standard microphysical properties for each of the 6 pure particle types that comprise the mixtures in the climatology (Table 3). These values are assumed; they probably represent the weakest link in the climatological retrieval we present. However, we have no vested interest in the choices made in Table 3. When performing retrievals with MISR observations rather than with simulations, we anticipate using additional constraints from *in situ* and field measurements whenever possible to reduce these uncertainties.

Based on mid-latitude simulations, for the assumed climatology, good viewing conditions, and moderate aerosol optical depth (nominally 0.5 at 0.55 microns wavelength), we find that MISR can retrieve optical depth fractional contributions of Sea Salt (large, spherical particles) and Accumulation Mode Dust (medium, non-spherical particles) to 20% or better. This is sufficient to distinguish Maritime from Continental aerosol air masses. MISR retrievals over dark water, using 9 angles and the red and near-IR channels, are not good at distinguishing Sulfates (medium, spherical, non-absorbing) from Carbonaceous particles (medium, spherical, absorbing); however, the sum of the fractional optical depth contributions for these two particle types is retrieved to 20% or better.

Coarse Mode Dust and Black Carbon particles contribute less than 20% to the total column aerosol optical depth everywhere in the climatology. Comparison models with adjusted amounts of other particle types can be found to meet the acceptance criterion for atmospheres containing these particles in most cases, though models with the correct composition usually yield the lowest χ^2_{max}.

In spite of the added flexibility offered by the climatological retrieval in allowing mixtures of particle types having different single scattering phase functions, constraints on total aerosol optical depth are nearly as tight as those for the generic retrieval. With atmospheric aerosol optical depth of 0.5, no comparison models with optical depth less than 0.4 or greater than 0.75 matched any of the atmospheres. The matching comparison models having optical depths greater than 0.60 all contain large fractions of Black Carbon, and most are isolated solutions that arise from fortuitous combinations of particle scattering phase functions. In an actual retrieval, such cases would be suspect, both because particle fractional optical depth contributions typically span a range of 5% to 20% near true solutions, and because mixtures containing 20% or more Black Carbon are climatologically unlikely.

When the total atmospheric aerosol column optical depth is reduced to 0.2, the constraints are looser than for the 0.5 cases, and some substitutions of particle types occur more readily. But the

ability to distinguish large, spherical particles (Sea Salt), non-spherical particles (Accumulation and Coarse Mode Dust), and small, dark particles (Black Carbon) is preserved, at least to within 20% or better of the expected values. And even with reduced sensitivity to particle microphysical properties, the total aerosol optical depth is constrained to 0.05 or better, if one rejects cases having implausibly large fractions of Black Carbon or Coarse Mode Dust.

Since the available cloud masks are unlikely to screen out optical depths of a few tenths or less of cirrus, we treat thin cirrus as an additional particle type. Climatological constraints on the spatial and temporal distribution of thin cirrus are so loose that by including it, we create an additional dimension in the sensitivity study. In most but not all cases, we can distinguish thin cirrus from other particle types in the climatology if the total column aerosol optical depth is greater than about 0.2 and the cirrus contribution is more than about 20%. The ability of MISR to identify aerosol Air Mass Types is significantly reduced when cirrus is present, but the sensitivity to total aerosol optical depth is not diminished.

We have sorted through an enormous amount of simulated data, and have identified patterns in MISR's sensitivity to atmospheric aerosols using both an average-particle "generic" approach, and a retrieval strategy that relies on an assumed climatology. It is time to look at real data. We anticipate that with instrument observations, uncertainties introduced by specific attributes of the environment will need to be considered: the vertical distribution of aerosols, the surface bi-directional reflectance function, and the actual physical properties of the aerosols and any cirrus ice crystals present. Where possible, we will rely on *in situ* and field measurements to help constrain the solution space. Analysis of observations from AirMISR, the aircraft version of our multi-angle instrument [*Diner et al.*, 1998b], is the subject of continuing work. And we hope some time soon to have data to study from MISR itself.

Acknowledgments. We thank Jeff Kiehl, Joyce Penner, Larry Stowe, and Ina Tegen for sharing their aerosol data with us, Sundar Christopher, Yoram Kaufman, Michael Mishchenko, Lorraine Remer, and Irina Sokolik for valuable discussions about particle properties, and David Diner and John Martonchik for discussions on a wide range of related scientific issues. This research is supported by the EOS-MISR instrument program, and by the Climate and Radiation Research and Analysis Program in the Earth Sciences Division of the National Aeronautics and Space Administration, under R. Curran. This work is performed at the Jet Propulsion Laboratory, California Institute of Technology, under contract with NASA.

References

Abdou, W.A., J.V. Martonchik, R. Kahn, R. West, and D. Diner, "A modified linear-mixing method for calculating atmospheric path radiances of aerosol mixtures", J. Geophys. Res. 102, 16,883-16,888 1997.

Andreae, M.O., Climatic effects of changing atmospheric aerosol levels, in A. Henderson-Sellers, ed., World Survey of Climatology, V.16: Future Climates of the World, Elsevier, New York, 341-392, 1995.

Bevington, P.R. and D. K. Robinson, Data reduction and error analysis for the physical sciences, Second edition, McGraw-Hill, New York, pp. 328, 1992.

Bruegge, C.J., V.G. Duval, N.L. Chrien, R.P. Korechoff, B.J. Gaitley, and E.B. Hochberg, MISR prelaunch instrument calibration and characterization results, IEEE Trans. Geosci. Remt. Sensing 36, 1186-1198, 1998.

Charlson, R.J., S. Schwartz, J. Hales, R. Cess, J. Coakley, Jr., J. Hansen, and D. Hofmann, Climate forcing by anthropogenic aerosols, *Science 255*, 423-430, 1992.

Chin, M., D.J. Jacob, G.M. Gardner, P.A. Spiro, M. Foreman-Fowler, and D.L. Savoie, A global three-dimensional model of tropospheric sulfate, J. Geophys. Res. 101, 18,669-18,690, 1996.

Cusack, S., A. Slingo, J.M. Edwards, and M. Wild, The radiative impact of a simple aerosol climatology on the Hadley Centre atmospheric GCM, Q.J.R. Meteorol. Soc. 124, 2517-2526, 1998.

d'Almeida, G.A., P. Koepke, and E.P. Shettle, Atmospheric Aerosols: Global climatology and radiative characteristics, Deepak Publishing, 1991.

Diner, D.J., J.C. Beckert, T.H. Reilly, C.J. Bruegge, J.E. Conel, R. Kahn, J.V. Martonchik, T.P. Ackerman, R. Davies, S.A.W. Gerstl, H.R. Gordon, J-P. Muller, R. Myneni, R.J. Sellers, B. Pinty, and M.M. Verstraete, Multiangle Imaging SptectrRadiometer (MISR) description and experiment overview, IEEE Trans. Geosci. Remt. Sensing 36, 1072-1087, 1998a.

Diner, D.J., L.M. Barge, C.J. Bruegge, T.G. Chrien, J.E. Conel, M.L. Eastwood, J.D. Garcia, M.A. Hernandez, C.G. Kurzweil, W.C. Ledeboer, N.D. Pignatano, C.M. Sarture, and B.G. Smith, The Airborne Multi-angle Imaging SpectroRadiometer (AirMISR): Instrument description and first results, IEEE Transact. Geosci. Rmt. Sensing 36, 1339-1349, 1998b.

Gao, B-C., A.F.H. Goetz, and W. Wiscombe, Cirrus cloud detection from airborne imaging spectrometer data using the 1.38 micron water vapor band, Geophys. Res. Lett. 20, 301-304, 1993.

Hanel, G., The properties of atmospheric aerosol particles as functions of relative humidity at thermodynamic equilibrium with the surrounding moist air, Adv. Geophys. 19, 73-188, 1976.

Hansen, J., M. Sato, A. Lacis, and R. Ruedy, The missing climate forcing, Philos. Trans. R. Soc. London, Ser. B, 352, 231-240, 1997.

Hansen, J.E., and L.D. Travis, Light scattering in planetary atmospheres, Space Sci. Rev. 16, 527-610, 1974.

Hartigan, J.A., and M.A. Wong, Algorithm AS 136: A K-means clustering algorithm, Applied Statistics 28, 100-108, 1979.

Haywood, J.M., V. Ramaswamy, and B.J. Soden, Tropospheric aerosol climate forcing in clear-sky satellite observations over the oceans, Science 283, 1299-1303, 1999.

Hegg, D., T. Larson, and P-F. Yuen, A theoretical study of the effect of relative humidity on light scattering by tropospheric aerosols, J. Geophys. Res. 98, 18,435-18,439, 1993.

Herman, J.R., P.K. Bhartia, O. Torres, C. Hsu, C. Seftor, and E. Celarier, Global distribution of UV-absorbing aerosols from Numbus 7 / TOMS data, J. Geophys. Res. 102, 16911-16922, 1997.

Husar, R.B., J.M. Prospero , and L.L. Stowe, Characterization of tropospheric aerosols over ocean with the NOAA advanced very high resolution radiometer optical thickness operational product, J. Geophys. Res. 102, 16889-16909, 1997.

Kahn, R., P. Banerjee, D. McDonald, and D. Diner, "Sensitivity of Multiangle imaging to Aerosol Optical Depth, and to Pure-Particle Size Distribution and Composition Over Ocean ", J. Geophys. Res., in press, 1998.

Kahn, R., R. West, D. McDonald, B. Rheingans, and M.I. Mishchenko, Sensitivity of multiangle remote sensing observations to aerosol sphericity, J. Geophys. Res. 102, 16861-16870, 1997.

Li, Z., L. Moreau, and A. Arking, On solar enerty disposition: A perspective from observation and modeling, Bull. Am. Meteoro. Soc. 78, 53-70, 1997.

Liousse, C., J. Penner, C. Chuang, J. Walton, H. Eddleman, and H. Cachier, A global three-dimensional model study of carbonaceous aerosols, J. Geopys. Res. 101, 19411-19432, 1996.

Martonchik, J.V., D.J. Diner, R. Kahn, M.M. Verstraete, B. Pinty, H.R. Gordon, and T.P. Ackerman, Techniques for the Retrieval of aerosol properties over land ocean using multiangle data, IEEE Trans. Geosci. Remt. Sensing 36, 1212-1227, 1998.

Minnis, P., K-N Liou, and Y. Takano, Inference of cirrus cloud properties using satellite-observed visible and Infrared radiances. Part II: Verification of theoretical cirrus radiative properties, *J. Atmosph. Sci. 50,* 1279-1304, 1993.

Mishchenko, M.I., W.B. Rossow, A. Macke, and A.A. Lacis, "Sensitivity of cirrus cloud albedo, bidirectional reflectance and optical thickness retrieval accuracy to ice particle shape," *J. Geophys. Res.101*, 16, 973-16, 985, 1996.

Mishchenko, M.I., L. Travis, R. Kahn, and R. West, "Modeling phase functions for dust-like tropospheric aerosols using a shape mixture of randomly oriented polydisperse spheroids," *J. Geophys. Res.102*, 16, 831-16, 847, 1997.

Penner, J.E., R.J. Charlson, J.M. Hales, N.S. Laulainen, R. Leifer, T. Novakov, J. Ogren, L.F. Radke, S.E. Schwartz, and L. Travis, Quantifying and minimizing uncertainty of climate forcing by anthropogenic aerosols, Bul. Am. Meteoro. Soc. 75, 375-400, 1994.

Prospero, J.M., R.J. Charlson, V. Mohnen, R. Jaenicke, A.C. Delany, J. Moyers, W. Zoller, and K. Rahn, The atmospheric aerosol system: An overview, Rev. Geophys. Space Phys. 21, 1607-1629, 1983.

Rao, C.R.N., L.L. Stowe, and E.P. McClain, Remote sensing of aerosols over the oceans using AVHRR data: Theory, practice and applications, Int. J. Remote Sensing 10, 743-749, 1989.

Reid, J.S., P.V. Hobbs, R.J. Ferek, D.R. Blake, J.V. Martins, M.R. Dunlap, and C. Liousse, Physical, chemical, and optical properties of regional hazes dominated by smoke in Brazil, *J. Geophys. Res.103*, 32,059-32,080, 1998.

Sassen, K., D. Starr, and T. Uttal, Mesoscale and microscale structure of cirrus clouds: Three case studies, *J. Atmosph. Sci. 46*, 371-396, 1989.

Mishchenko, M.I., W.B. Rossow, A. Macke, and A.A. Lacis, "Sensitivity of cirrus cloud albedo, Shettle, E.P., and R.W. Fenn, Models for the aerosols of the lower atmosphere and te effects of humidity variations on their optical properties, AFGL-TR-79-0214, Air Force Geophysics Laboratory, pp.94, 1979.

Sokolik, I.N., and O.B. Toon, Direct radiative forcing by anthropogenic airborne mineral aerosols, *Nature 381*, 681-683, 1996.

Stowe, L.L., A.M. Ignatov, and R.R. Singh, Development, validation, and potential enchancements to the second-generation operational aerosol product at the National Environmental Satellite, Data, and Information Service of the National Oceanic and Atmospheric Administration, *J. Geophys. Res. 102*, 16923-16934, 1997.

Tegen, I., P. Hollrig, M. Chin, I. Fung, D. Jacob, and J. Penner, Contribution of different aerosol species to the global aerosol extinction optical thickness: Estimates from model results, J. Geophys. Res. 102, 23,895-23,915, 1997.

Tegen, I., and I. Fung, Contribution to the atmospheric mineral aerosol load from land surface modification, J. Geophys. Res. 100, 18707-18726, 1995.

World Climate Programme WCP-112. A Preliminary Cloudless Standard Atmosphere for Radiation Computation. IAMAP (International Association for Meteorology and Atmospheric Physics), Boulder, CA, pp.53, 1984.

Table 1. Some Characteristics of the Monthly, Global Aerosol Results Adopted for this Study

Aerosol Type	Source	Reference	Spatial Resolution	Quantities Reported	Units Given	Factor Used to Convert Mass to τ
Accumulation and Coarse Mineral Dust [†]	GISS	Tegen & Fung (1995)	4° x 5°	Total Column Dust Optical Depth, regrouped into 2 size bins: < 1 micron (accumulation), 1 to 10 micron (coarse)	none	1.5 m^2/gm (accumulation mode); 0.3 x m^2/gm (coarse mode)
Sea Salt[†]	GISS	Tegen et al. (1997)	4° x 5°	Total Column Aerosol Optical Thickness	none	0.3 m^2/gm
Sulfates[§]	LLNL	Liousse et al. (1996)	~ 4.5° x 7.5°	Column Mass Load	g/m^2	8.5 m^2/gm
Carbonaceous Particles[†]	GISS	Liousse et al. (1996)	4° x 5°	Total Column Aerosol Optical Thickness	none	8.0 m^2/gm
Black Carbon[†]	GISS	Liousse et al. (1996)	4° x 5°	Total Column Aerosol Optical Thickness	none	9. m^2/gm
Total Aerosol[£] (assumes "Sulfate" optical properties)	NOAA/ AVHRR	Stowe et al. (1997)	1° x 1° Global Oceans +70° to -70° latitude	Total Column Optical Depth (at 0.63 μm)	none	Optical depth adjustment applied $\tau' = 1.56\,\tau + 0.03$
Sulfates[†]	GISS	Chin et al. (1996)	4° x 5°	Total Column Aerosol Optical Thickness	none	6.0 m^2/gm (land) 10 m^2/gm (ocean)

[†]These data were obtained from Ina Tegen et al., Goddard Institute of Space Studies (GISS), 1997. web site (http:// www.giss.nasa.gov/gacp/transport/).

[§]These data were obtained from Joyce Penner et al., from the Lawrence Livermore National Laboratory (LLNL) model, personal communication, 1998.

[£]These data were obtained from Larry Stowe et al., National Oceanographic and Atmospheric Administration (NOAA), personal communication, 1997.

Table 2. Climatological Mixing Groups and Representative Air Mass Types[‡]

Classification	Component 1	Component 2	Component 3	Component 4	Notes
1. Carbonaceous + Dusty Maritime	**Sulfate**	**Sea Salt**	**Carbon-aceous**	**Accum. Dust**	34% of voxels are non-zero
1a.	**0.67**	0.13	0.10	0.10	Mid-high latitude oceans, winter: Nov.-May, southern oceans; May-Sept., North Atlantic.
1b.	0.41	0.13	**0.27**	**0.19**	Tropical to sub-tropical oceans, all year; June-Oct., remote southern oceans.
1c.	0.40	**0.32**	0.17	0.11	Southern mid-latitude oceans, all year; Nov.-March, remote southern oceans.
2. Dusty Maritime + Coarse Dust	**Sulfate**	**Sea Salt**	**Accum. Dust**	**Coarse Dust**	14% of voxels are non-zero
2a.	**0.52**	0.17	0.21	0.10	Downwind of deserts: Australia, Africa, S. America, peak during southern summer; Oct.-Jan., N.W. Africa.
2b.	0.29	0.13	**0.39**	**0.19**	Same pattern as 2a, but closer to continental source regions.
3. Carbonaceous + Black Carbon Maritime	**Sulfate**	**Sea Salt**	**Carbon-aceous**	**Black Carbon**	11% of voxels are non-zero
3a.	**0.51**	0.18	0.26	0.05	Ocean near Indonesia, all year; Dec.-March, North Atlantic; Jan.-Feb., oceans near central Africa; May-July, oceans near tropical S. America; July-Sept., oceans near central America.
3b.	0.35	0.10	**0.47**	**0.08**	Same pattern as 3a, but closer to continental source regions.

4. Carbonaceous + Dusty Continental	**Sulfate**	**Accum. Dust**	**Coarse Dust**	**Carbon-aceous**	21% of voxels are non-zero
4a.	**0.61**	0.21	0.05	0.13	Feb.-Nov., eastern N. America; July-Sept., western N. America; Jan.-March, S. America; Jan.-March, S. Africa; Oct., India; July-Oct., Korea.
4b.	0.40	**0.35**	0.09	**0.16**	March-July, Oct.-Nov, western N. America; Sept.-Dec., S. America; April-Oct., S. Africa; Jan.-March, central Asia; April-June, Nov.-Dec., Korea.
4c.	0.22	**0.51**	**0.16**	0.11	Arabia and N. Africa, all year; Nov-Dec., S. Africa; March-Dec., central Asia; Jan.-April, July-Dec., Australia.
5. Carbonaceous + Black Carbon Continental	**Sulfate**	**Accum. Dust**	**Carbon-aceous**	**Black Carbon**	15% of voxels are non-zero
5a.	**0.59**	0.12	0.23	0.06	April-Oct., Europe; Jan.-March, N. Asia; July-Sept., E. China; Nov.-March, E. North America; Nov.-March, equatorial S. America.
5b.	0.25	0.12	**0.54**	0.09	Tropical-subtropical Africa, all year; Dec.-March, W. Europe; Jan.-March, N. Asia; Jan.-March, E. China.
5c.	0.44	**0.23**	**0.26**	0.07	Nov.-Jan., W. Europe; Oct.-March, E. Europe; Nov.-Feb., N. Asia; Oct.-Dec., April-July, E. China; Dec.-April, equatorial S. America.

‡ Relative abundances are given as fractions of the total optical depth in MISR Band 2 (558 nm effective wavelength). Numbers in bold are distinctive constituents of the mixture. "Accum. Dust" stands for Accumulation Mode Dust.

Table 3. Pure Particle Types Assumed for Climatology*

Aerosol Type	r_1 (μm)	r_2 (μm)	r_c (μm)	σ	n_r (MISR band)	n_i (MISR band)	ω_0 (670 nm)	RH (%)	Particle Size/Shape Category
Sulfate (Accum.) over Land	(0.007) 0.007	(0.7) 0.81	(0.07) 0.08	(1.86) 1.88	(1.53) 1.46	0.0 (all)	1.0	(0) 70	Medium Spherical
Sulfate (Accum.) over Ocean	(0.007) 0.008	(0.7) 1.05	(0.07) 0.10	(1.86) 1.87	(1.53) 1.39	0.0 (all)	1.0	(0) 80	Medium Spherical
Sea Salt (Accum.)	(0.05) 0.098	(1.0) 1.98	(0.35) 0.61	(2.51) 2.29	(1.50) 1.35	0.0 (all)	1.0	(0) 80	Large Spherical
Mineral Dust† (Accum.)	0.05	2.0	0.47	2.60	1.53	0.0085(1) 0.0055(2) 0.0045(3) 0.0012(4)	0.91	--	Medium Non-spherical
Mineral Dust† (Coarse)	0.5	15.0	1.90	2.60	1.53	0.0085(1) 0.0055(2) 0.0045(3) 0.0012(4)	0.73	--	Large Non-spherical
Carbon-aceous††	0.007	2.0	0.13	1.80	1.50	0.025 (all)	0.87	97	Medium Spherical
Black Carbon	0.001	0.5	0.012	2.00	1.75	0.455(1) 0.440(2) 0.435(3) 0.430(4)	0.17	--	Small
Thin Cirrus‡‡	3.0	200.	--	--	1.316(1) 1.311(2) 1.308(3) 1.304(4)	0.0 (all)	1.0	100	Very large Fractal

*In this table, r_1 and r_2 are the lower and upper radius limits for the particle size distribution. "Accum." stands for "Accumulation Mode" particles. Particle types are distributed log-normally, with characteristic radius r_c and width σ. ω_0 is the single scattering albedo, given here at the effective wavelength of the MISR red channel. RH is the relative humidity to which hygroscopic particles are hydrated. Sulfate and Sea Salt particles are hydrated to the RH value in the "RH" column using the model of *Hanel* [1976]; where properties for these particle types are in parentheses, they refer to the dry particles. The aerosol physical data are abstracted from *Shettle and Fenn* [1979], *d'Almeida et al.* [1991], *WCP* [1984], and other sources, except as indicated. Optical data for spherical particles are calculated using standard Mie theory.

† Non-spherical (mixed spheroid) mineral dust models based on *Mishchenko et al.* [1997].

†† Carbonaceous particle model based on *Reid et al.* [1998].

‡‡ Fractal thin cirrus model based on *Mishchenko et al.* [1996].

Table 4. Mixing Groups and Air Masses Containing Thin Cirrus[‡]

Classification	Component 1	Component 2	Component 3	Component 4
1C. Cirrus + Carbonaceous Maritime	**Sulfate**	**Sea Salt**	**Carbon-aceous**	**Cirrus**
1Ca.1	**0.55**	0.10	**0.25**	0.10
1Ca.2	**0.51**	0.08	**0.21**	0.20
1Ca.5	**0.30**	0.05	**0.15**	0.50
1Cb.1	**0.45**	**0.35**	0.10	0.10
1Cb.2	**0.40**	**0.30**	0.10	0.20
1Cb.5	**0.27**	**0.18**	0.05	0.50
2C. Cirrus + Dusty Maritime	**Sulfate**	**Sea Salt**	**Accum. Dust**	**Cirrus**
2Ca.1	**0.55**	0.15	0.20	0.10
2Ca.2	**0.52**	0.11	0.17	0.20
2Ca.5	**0.30**	0.08	0.12	0.50
2Cb.1	0.25	0.10	**0.55**	0.10
2Cb.2	0.21	0.08	**0.51**	0.20
2Cb.5	0.10	0.05	**0.35**	0.50
3C. Cirrus + Black Carbon Maritime	**Sulfate**	**Sea Salt**	**Black Carbon**	**Cirrus**
3Ca.1	**0.65**	0.15	**0.10**	0.10
3Ca.2	**0.60**	0.10	**0.10**	0.20
3Ca.5	**0.37**	0.08	**0.05**	0.50

4C. Cirrus + Carbonaceous Continental	Sulfate	Accum. Dust	Carbon-aceous	Cirrus
4Ca.1	**0.55**	0.10	0.25	0.10
4Ca.2	**0.50**	0.08	0.22	0.20
4Ca.5	**0.30**	0.05	0.15	0.50
4Cb.1	0.25	0.10	**0.55**	0.10
4Cb.2	0.22	0.08	**0.50**	0.20
4Cb.5	0.15	0.05	**0.30**	0.50
5C. Cirrus + Dusty Continental	**Sulfate**	**Accum. Dust**	**Coarse Dust**	**Cirrus**
5Ca.1	0.25	**0.50**	0.15	0.10
5Ca.2	0.22	**0.45**	0.13	0.20
5Ca.5	0.15	**0.25**	0.10	0.50
6C. Cirrus + Black Carbon Continental	**Sulfate**	**Accum. Dust**	**Black Carbon**	**Cirrus**
6Ca.1	**0.55**	0.25	**0.10**	0.10
6Ca.2	**0.50**	0.20	**0.10**	0.20
6Ca.5	**0.27**	0.18	**0.05**	0.50

Figure Captions

Plate 1. (a through d) Global maps for January, April, July, and October, respectively, showing the spatial distribution of the 5 aerosol mixing groups defined as major headings in Table 2, based on the aggregate of aerosol transport models listed in Table 1. Blue areas correspond to "Carbonaceous + Dusty Maritime," Yellow to "Dusty Maritime + Coarse Dust," Green to "Carbonaceous + Black Carbon Maritime," Brown to "Carbonaceous + Dusty Continental," and Gray to "Carbonaceous + Black Carbon Continental. (e through h) Global maps for January, April, July, and October, respectively, showing the spatial distribution of the 13 representative air mass types, defined in Table 2. To obtain these maps, each point was first classified by aerosol mixing group, and then sub-classified according to the representative air mass type nearest it, using percent contributions to total column optical depth of each component as the 4-dimensional, linear distance metric.

Plate 2. Example of sections through a 4-dimensional histogram, showing clustering in the climatological proportions over a year of the aerosol components for Mixing Group 4 ("Carbonaceous + Dusty Continental" in Table 2). This mixing group includes Sulfate, Accumulation Mode Dust, Coarse Mode Dust and Carbonaceous particles. Shown here are 6 planes with constant Coarse Mode Dust fraction, corresponding to bins with (a) 25% to 30%, (b) 20% to 25%, (c) 15% to 20%, (d) 10% to 15%, (e) 5% to 10%, and (f) 0% to 5% Coarse Mode Dust, respectively. Red shades indicate high counts (>2500), gray are intermediate values (about 1200 to 2500), light blue values range from 600 to 1200, dark blue are counts below 600, and black are locations for which there were no mixtures in the climatology falling in that mixture bin. Below each section are numerical values of the number of hits, and the average fraction of each component, for the most heavily populated pixel in that section. See text for further details.

Plate 3. (a through d) Global maps of total column aerosol optical depth for January, April, July, and October, respectively, based on the transport models of *Tegen et al.*[1997]. (e through h) Difference maps between AVHRR-derived total column aerosol optical depth for 1989 [*Stowe et al.*, 1997] and the corresponding monthly transport model results for January, April, July, and October, respectively.

Plate 4. Example of sections through a tetrahedral comparison matrix. Airmass Type 2a (Table 2) defines the aerosol composition of the atmosphere, and the comparison models are all 1771 combinations of Sulfate, Sea Salt, Accumulation Mode Dust, and Coarse Mode Dust, in 5% increments, that define Mixing Group 2. In this figure, the optical depth in MISR Band 2 is set to 0.5 for both the atmosphere and comparison models, and typical MISR mid-latitude geometry is adopted. Shown here are 6 planes with constant Coarse Mode Dust fraction, corresponding to (a) 0%, (b) 5%, (c) 10%, (d) 15%, (e) 20%, and (f) 25% Coarse Mode Dust, respectively. Each pixel is divided into 5 fields; the 4 sub-pixels are colored to indicate the results of 4 chi-squared tests comparing the atmosphere and one comparison model. The background is colored with the result of the largest (most sensitive) of the 4 tests. A blue pixel indicates that within instrument uncertainty, the associated comparison model must be accepted. Below each section are listed the maximum test value (χ^2_{max}), and the corresponding fraction of each component, for the comparison model with the smallest χ^2_{max}, suggesting that this model that matches the atmosphere most closely. See text for further details.

Plate 5. (a-d) Same as Plate 4, but for an atmosphere with aerosol composition given by Air Mass Type 4a (Table 2) and comparison models defined by Mixing Group 4 (Carbonaceous + Dusty Continental, Table 2). Shown here are 4 planes with constant Coarse Mode Dust fraction, corresponding to (a) 0%, (b) 5%, (c) 10%, (d) 15%, respectively.

(e-h) Same as Plate 5 (a-d), but with the atmosphere defined by Air Mass Type 4c. The 4 planes shown are sections with constant Coarse Mode Dust fraction, corresponding to (e) 10%, (f)

15%, (g) 20%, (h) 25%, respectively. Air Mass Type 4c contains 39% less Sulfate, 30% more Accumulation Mode Dust, and 11% more Coarse Mode Dust, than Air Mass Type 4a.

Figure 1. Single scattering phase functions for 6 particle types (including 2 hydration states for Sulfate particles) and thin cirrus. Detailed physical properties for these particles are given in Table 3. Superposed on this plot are the scattering angles sampled by the 9 MISR cameras for a typical mid-latitude case. Camera designations are "A," B," "C," and "D," for the 4 groups of cameras viewing at shallow and more steep emission angles, and "f" for forward-looking, "a" for aft-looking, and "n" for nadir-viewing cameras.

Figure 2. Whisker plot matrix showing MISR sensitivity to all 13 Representative Air Mass Types, as compared with every combination on 5% tetrahedral grids for all 5 Mixing Groups. Each column contains plots for one Air Mass Type in Table 2. The first 5 rows are for each of the Mixing Groups in Table 2. The horizontal axis in each plot allows 6 positions for whiskers, one for each pure particle type in the climatology (Tables 1 and 3). The vertical axis in each plot indicates the fraction of column optical depth in MISR Band 2 contributed by a particle type. Each plot summarizes the comparisons between an atmosphere with the aerosol mixture defined by one Air Mass Type, and all 1771 comparison models in one Mixing Group. Whiskers are drawn spanning the upper and lower limits of fractional contribution of each particle type in the Mixing Group, for any model that meets the criterion $\chi^2_{max} < 1$. Fractions of component particle contributions for the comparison model yielding the smallest value of χ^2_{max} are marked by "x" symbols on each whisker. The last row of plots indicate with "+" signs the fractions of constituents in the Air Mass Types. For this plot matrix, the total column optical depth in MISR Band 2 is set to 0.5 for all atmospheres and comparison models, and cosine of the solar zenith angle is set to 0.6, a typical MISR mid-latitude situation. See text for further details.

Figure 3. Same as Figure 2, but for a mid-latitude case with atmospheric (Air Mass) total column aerosol optical depths of 0.5 in MISR Band 2, and comparison model (Mixing Group) optical depths of 0.65.

Figure 4. Same as Figure 2, but for a mid-latitude case with all atmospheric and comparison model total column aerosol optical depths set to 0.2 in MISR Band 2.

Figure 5. Same as Figure 2, but for a mid-latitude case with atmospheric (Air Mass) total column aerosol optical depths of 0.20 in MISR Band 2, and comparison model (Mixing Group) optical depths of 0.30.

Figure 6. Whisker plot matrix showing MISR sensitivity to 9 Representative Air Mass Types each containing 50% cirrus (Table 4), as compared with every combination on 5% tetrahedral grids for 5 Mixing Groups that do not contain cirrus (Table 2). This is a mid-latitude case, for which the total aerosol (including cirrus) column optical depth is 0.5 in MISR Band 2.

Figure 7. Plot of the simulated single scattering contribution to the equivalent reflectance at each of the 9 MISR cameras. The curves labeled 3 or 4 with subscript "A" show equivalent reflectances for an atmosphere containing Air Mass Type C1b.5, which is 50% cirrus (Table 4), for MISR wavelength Bands 3 and 4, respectively. The curves labeled 3 or 4 with subscript "C" are for a comparison model in Mixing Group 4 (Table 2) containing 65% Sulfate, 15% Accumulation Mode Dust, 10% Coarse Mode Dust, and 10% Carbonaceous particles. This is a mid-latitude case, and the MISR Band 2 total particle column optical depth is 0.5 for both atmosphere and comparison model. The two lower curves, labeled $\Delta 3$ and $\Delta 4$, are the camera-by-camera reflectance differences between the atmosphere and comparison model for MISR Bands 3 and 4, respectively.

Figure 8. Whisker plot matrix showing MISR sensitivity to 9 Representative Air Mass Types each containing 20% cirrus, as compared with every combination on 5% tetrahedral grids for 6 Mixing Groups that also contain cirrus (see Table 4). This is a mid-latitude case, for which the total aerosol (including cirrus) column optical depth is 0.5 in MISR Band 2.

a

e

b

f

c

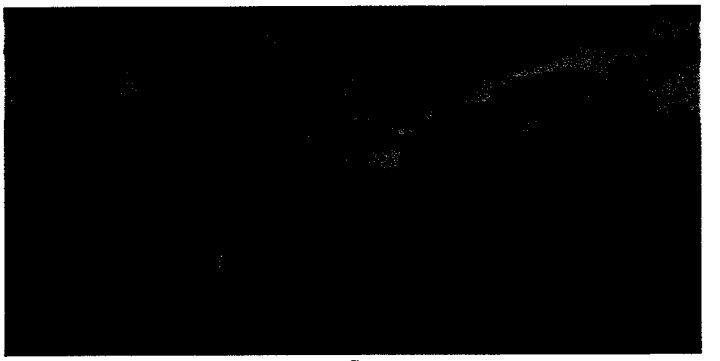

g

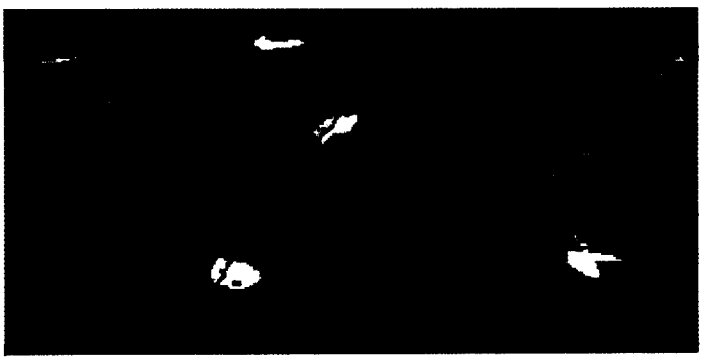

d

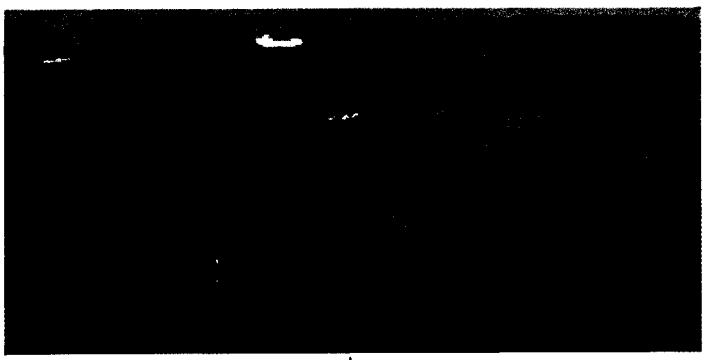

h

- Carbonaceous + Dusty Maritime
- Dusty Maritime + Coarse Dust
- Carbonaceous + Black Carbon Maritime
- Carbonaceous + Dusty Continental
- Carbonaceous + Black Carbon Continental

- Carbonaceous + Dusty Maritime (1a)
- Carbonaceous + Dusty Maritime (1b)
- Carbonaceous + Dusty Maritime (1c)
- Dusty Maritime + Coarse Dust (2a)
- Dusty Maritime + Coarse Dust (2b)
- Carbonaceous + Black Carbon Maritime (3a)
- Carbonaceous + Black Carbon Maritime (3b)
- Carbonaceous + Dusty Continental (4a)
- Carbonaceous + Dusty Continental (4b)
- Carbonaceous + Dusty Continental (4c)
- Carbonaceous + Black Carbon Continental (5a)
- Carbonaceous + Black Carbon Continental (5b)
- Carbonaceous + Black Carbon Continental (5c)

Iso "coarse dust" planes

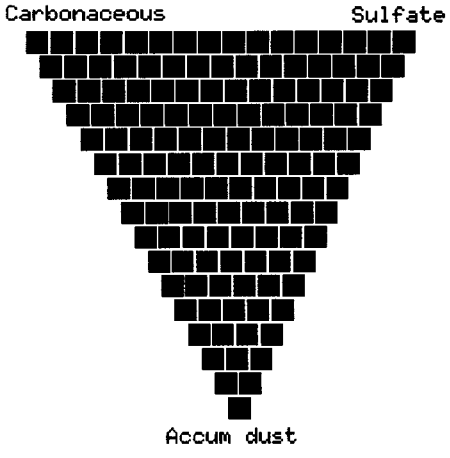

value = 507
Accum dust (average %) = 0.567155
Coarse dust (average %) = 0.270206
Sulfate (average %) = 0.122490
Carbonaceous (average %) = 0.040148

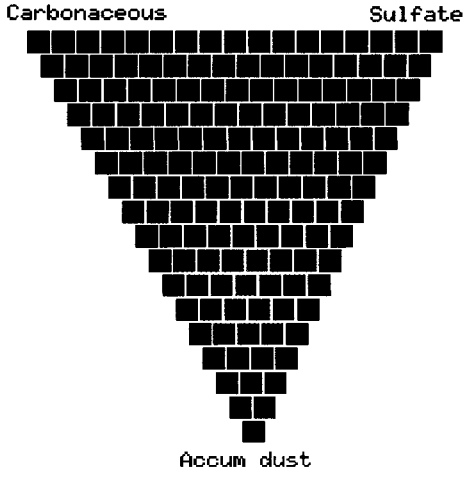

value = 972
Accum dust (average %) = 0.525378
Coarse dust (average %) = 0.227370
Sulfate (average %) = 0.177022
Carbonaceous (average %) = 0.070230

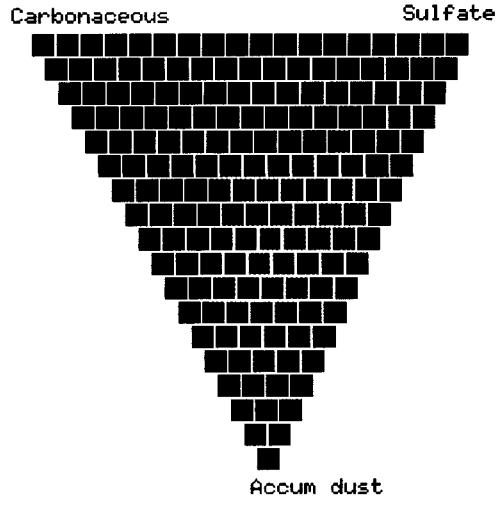

value = 1797
Accum dust (average %) = 0.526797
Coarse dust (average %) = 0.173202
Sulfate (average %) = 0.229469
Carbonaceous (average %) = 0.070532

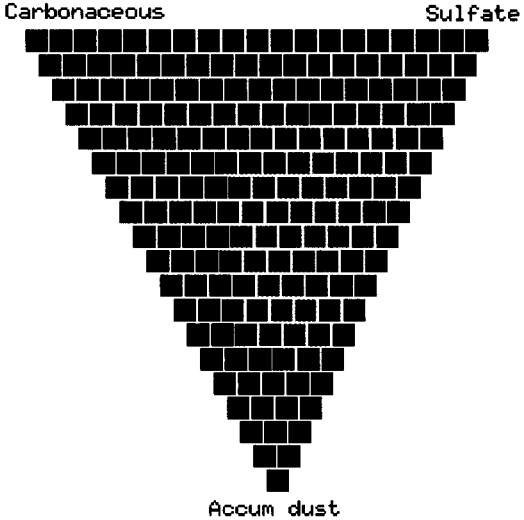

value = 4222
Accum dust (average %) = 0.425491
Coarse dust (average %) = 0.124157
Sulfate (average %) = 0.325009
Carbonaceous (average %) = 0.125343

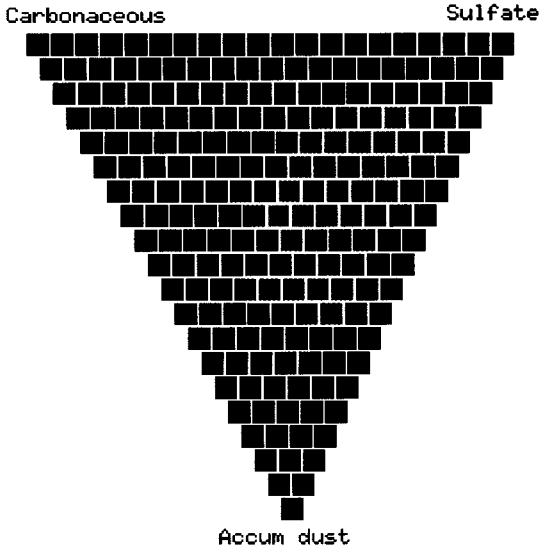

value = 5895
Accum dust (average %) = 0.324137
Coarse dust (average %) = 0.071466
Sulfate (average %) = 0.473780
Carbonaceous (average %) = 0.130618

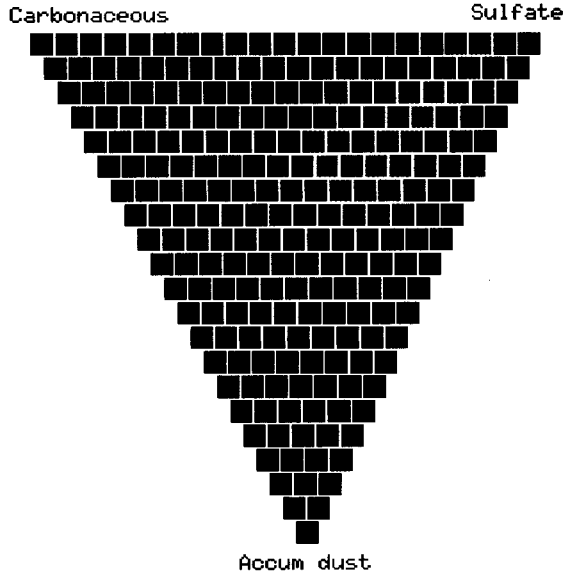

value = 4947
Accum dust (average %) = 0.230861
Coarse dust (average %) = 0.039723
Sulfate (average %) = 0.573630
Carbonaceous (average %) = 0.155785

a
b
c
d
e
f
g
h
Tau > 0.8
0.5 < Tau <= 0.8
0.3 < Tau <= 0.5
0.2 < Tau <= 0.3
0.15 < Tau <= 0.2
0.1 < Tau <= 0.15
0.08 < Tau <= 0.1
0.05 < Tau <= 0.08
0.03 < Tau <= 0.05
Tau <= 0.03
Missing data
-0.3
<-0.3
-0.15
0.0
0.25
>0.5
0.5

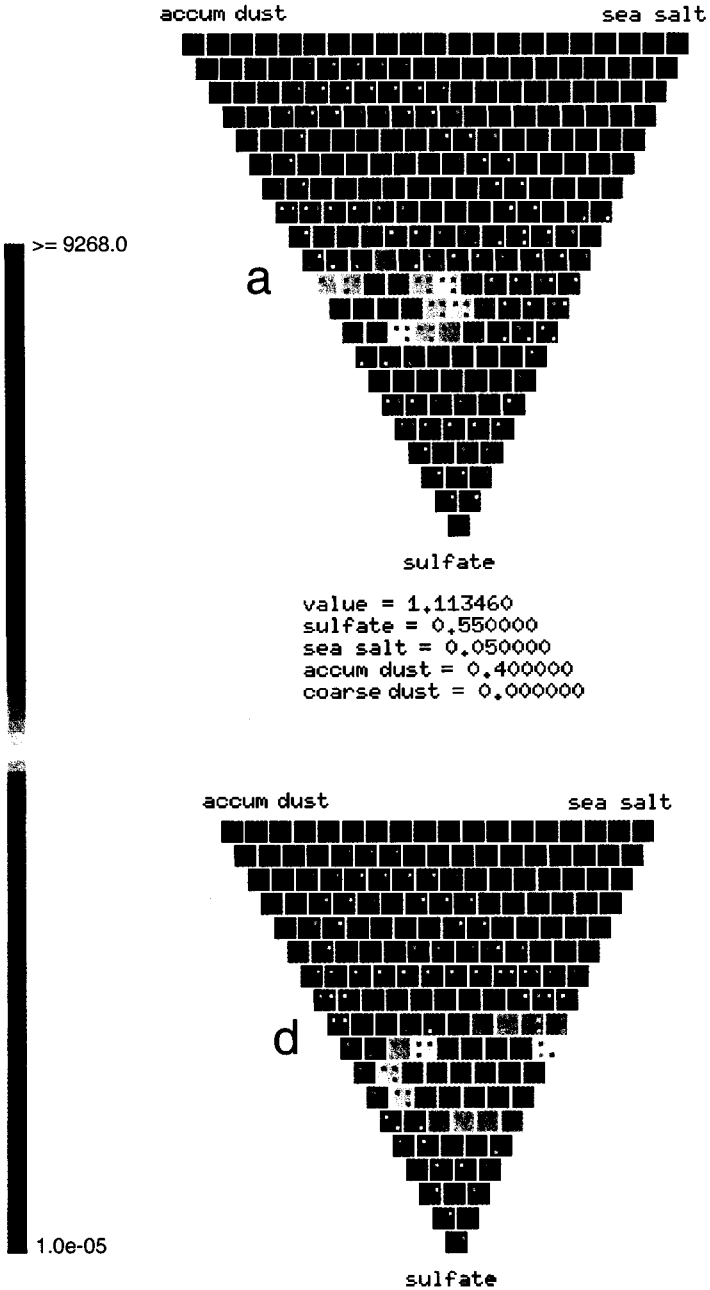
>= 9268.0
1.0e-05
accum dust
sea salt
a
sulfate
value = 1.113460
sulfate = 0.550000
sea salt = 0.050000
accum dust = 0.400000
coarse dust = 0.000000
accum dust
sea salt
b
sulfate
value = 0.341243
sulfate = 0.550000
sea salt = 0.100000
accum dust = 0.300000
coarse dust = 0.050000
accum dust
sea salt
c
sulfate
value = 0.174857
sulfate = 0.500000
sea salt = 0.200000
accum dust = 0.200000
coarse dust = 0.100000
accum dust
sea salt
d
sulfate
value = 0.387070
sulfate = 0.500000
sea salt = 0.200000
accum dust = 0.150000
coarse dust = 0.150000
accum dust
sea salt
e
sulfate
value = 0.862153
sulfate = 0.500000
sea salt = 0.250000
accum dust = 0.050000
coarse dust = 0.200000
accum dust
sea salt
f
sulfate
value = 2.168558
sulfate = 0.500000
sea salt = 0.250000
accum dust = 0.000000
coarse dust = 0.250000

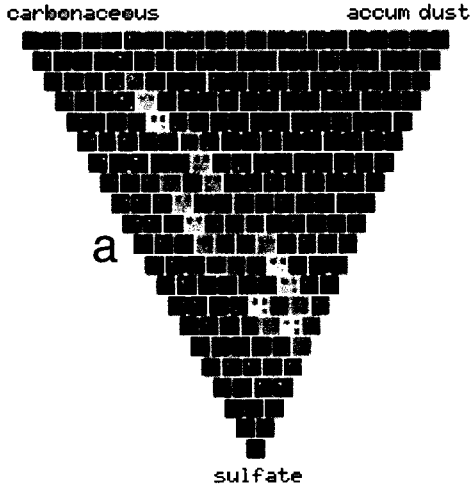

value = 0.433158
sulfate = 0.50
accum dust = 0.25
carbonaceous = 0.25
coarse dust = 0.00

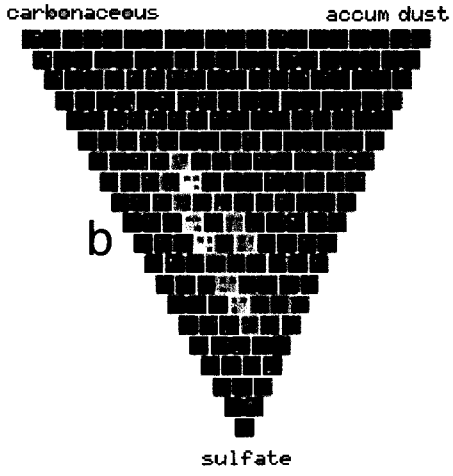

value = 0.058997
sulfate = 0.60
accum dust = 0.20
carbonaceous = 0.15
coarse dust = 0.05

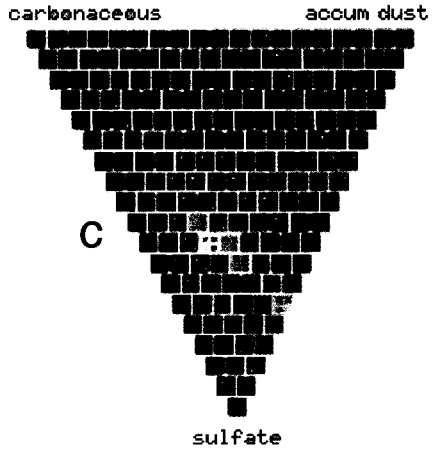

value = 0.334815
sulfate = 0.70
accum dust = 0.20
carbonaceous = 0.00
coarse dust = 0.10

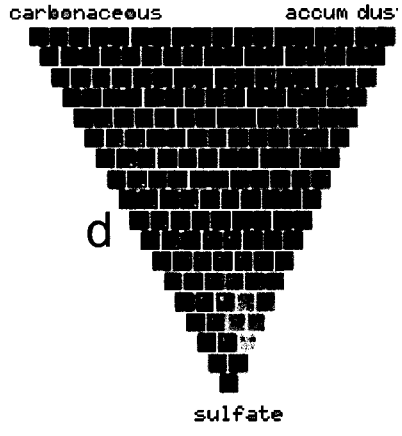

value = 2.486767
sulfate = 0.70
accum dust = 0.15
carbonaceous = 0.00
coarse dust = 0.15

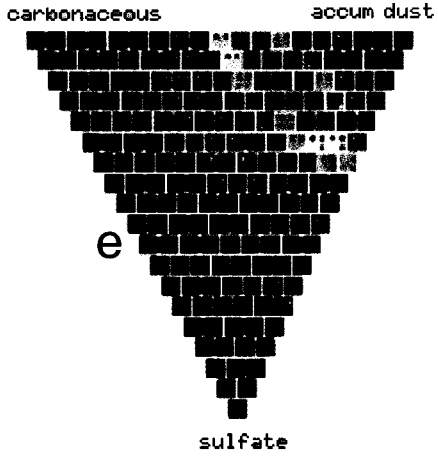

value = 0.261991
sulfate = 0.05
accum dust = 0.55
carbonaceous = 0.30
coarse dust = 0.10

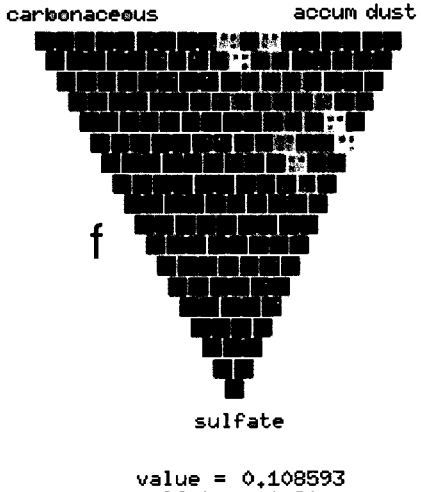

value = 0.108593
sulfate = 0.20
accum dust = 0.50
carbonaceous = 0.15
coarse dust = 0.15

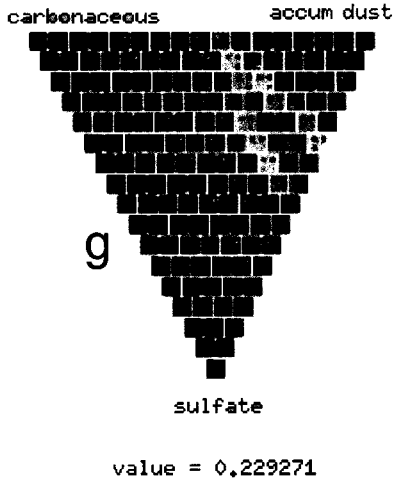

value = 0.229271
sulfate = 0.30
accum dust = 0.50
carbonaceous = 0.00
coarse dust = 0.20

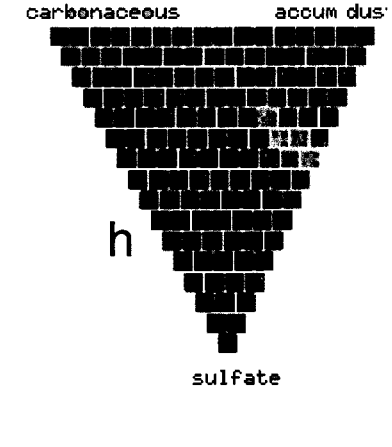

value = 2.019287
sulfate = 0.35
accum dust = 0.40
carbonaceous = 0.00
coarse dust = 0.25

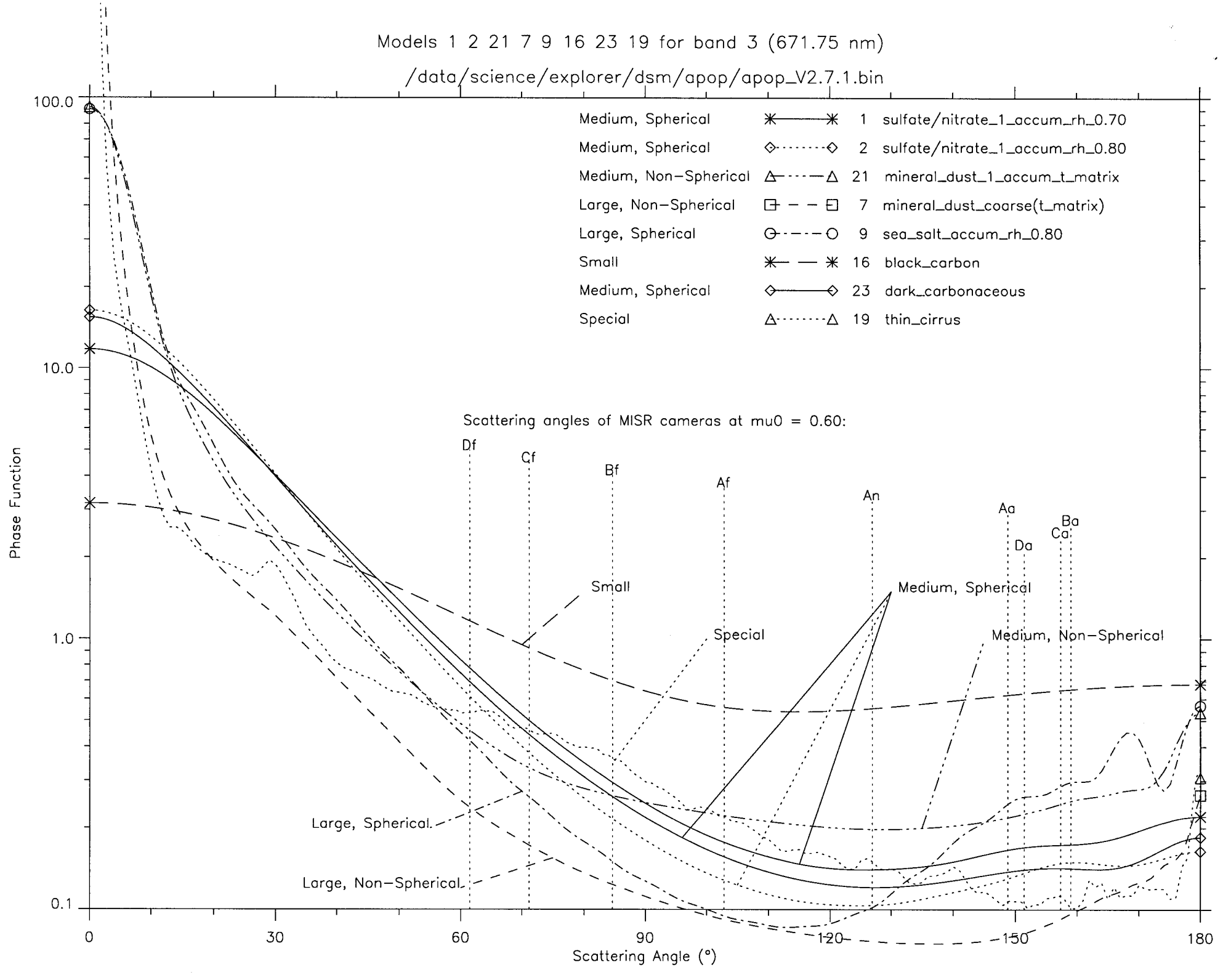
Models 1 2 21 7 9 16 23 19 for band 3 (671.75 nm)
/data/science/explorer/dsm/apop/apop_V2.7.1.bin
Medium, Spherical 1 sulfate/nitrate_1_accum_rh_0.70
Medium, Spherical 2 sulfate/nitrate_1_accum_rh_0.80
Medium, Non-Spherical 21 mineral_dust_1_accum_t_matrix
Large, Non-Spherical 7 mineral_dust_coarse(t_matrix)
Large, Spherical 9 sea_salt_accum_rh_0.80
Small 16 black_carbon
Medium, Spherical 23 dark_carbonaceous
Special 19 thin_cirrus
Scattering angles of MISR cameras at mu0 = 0.60:
Df
Cf
Bf
Af
An
Aa
Da
Ca
Ba
Small
Special
Medium, Spherical
Medium, Non-Spherical
Large, Spherical
Large, Non-Spherical
Phase Function
100.0
10.0
1.0
0.1
0
30
60
90
120
150
180
Scattering Angle (°)

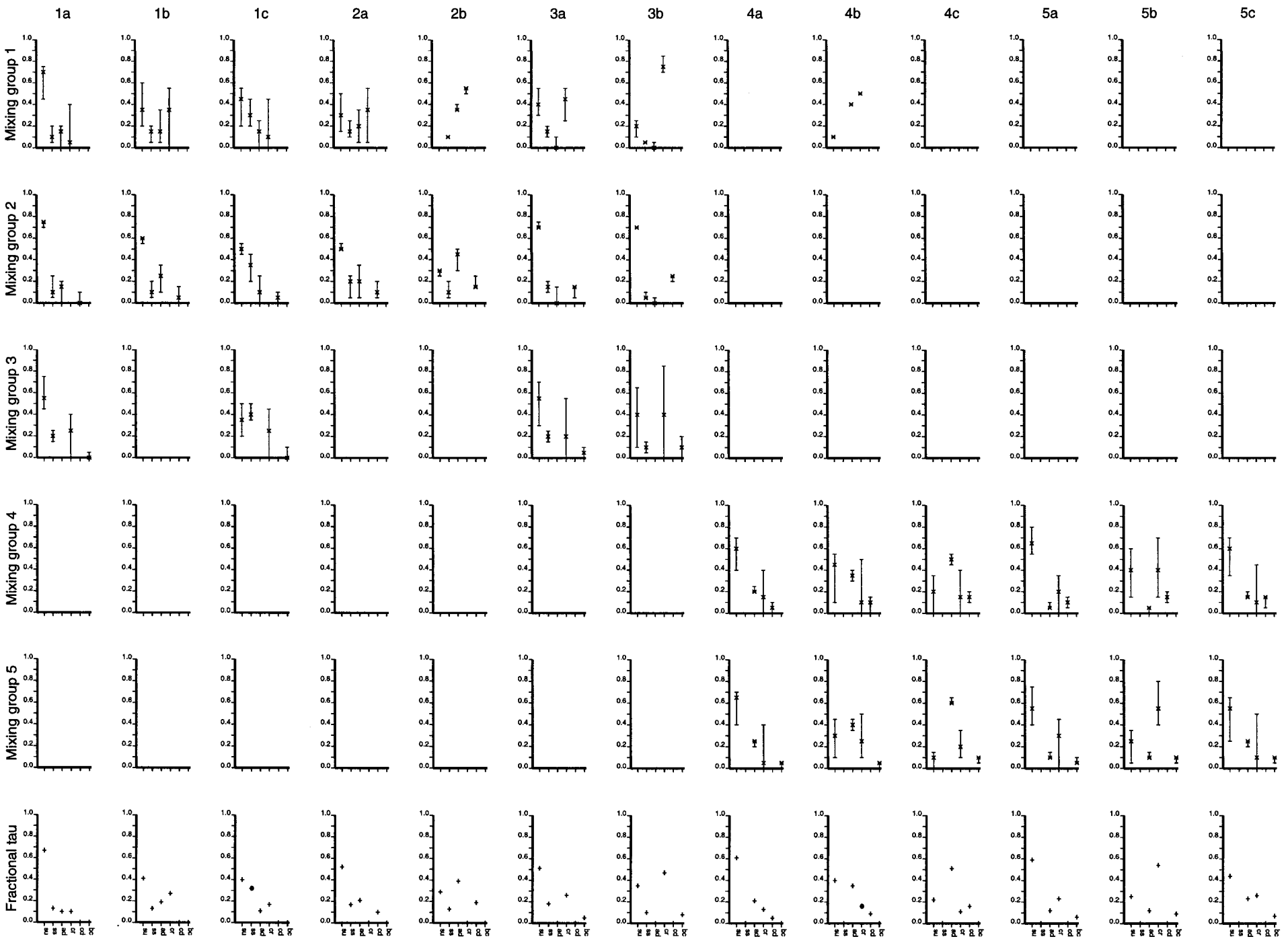
1a
1b
1c
2a
2b
3a
3b
4a
4b
4c
5a
5b
5c
Mixing group 1
Mixing group 2
Mixing group 3
Mixing group 4
Mixing group 5
Fractional tau
su := sulfate; ss := sea salt; ad := accumulation dust; cr := carbonaceous; cd := coarse dust; bc := black carbon
tau_atm = 0.50, tau_comp = 0.50, mu0 = 0.6

Fig. 2

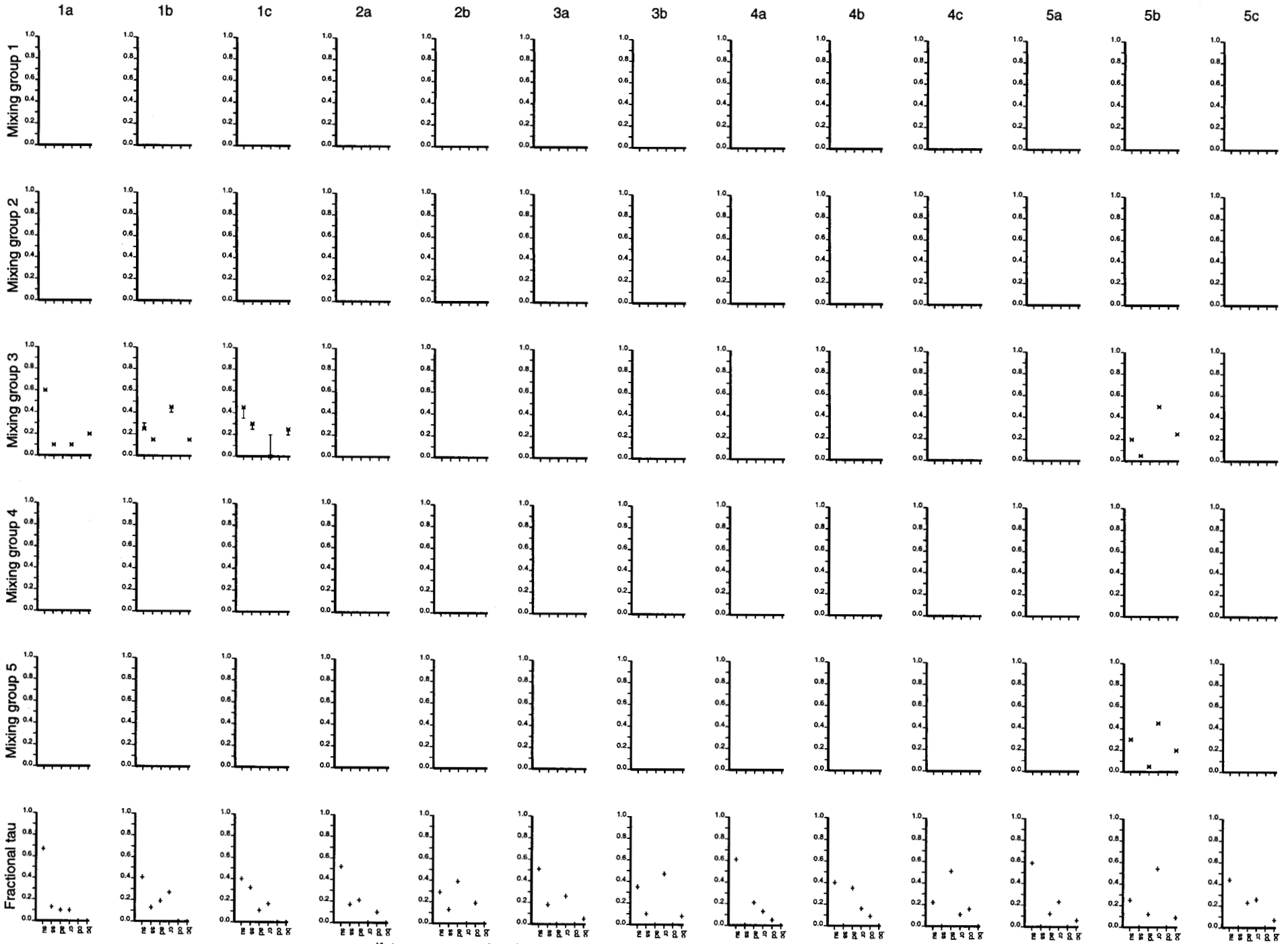

su := sulfate; ss := sea salt; ad := accumulation dust; cr := carbonaceous; cd := coarse dust; bc := black carbon

tau_atm = 0.50, tau_comp = 0.65, mu0 = 0.6

Fig. 3

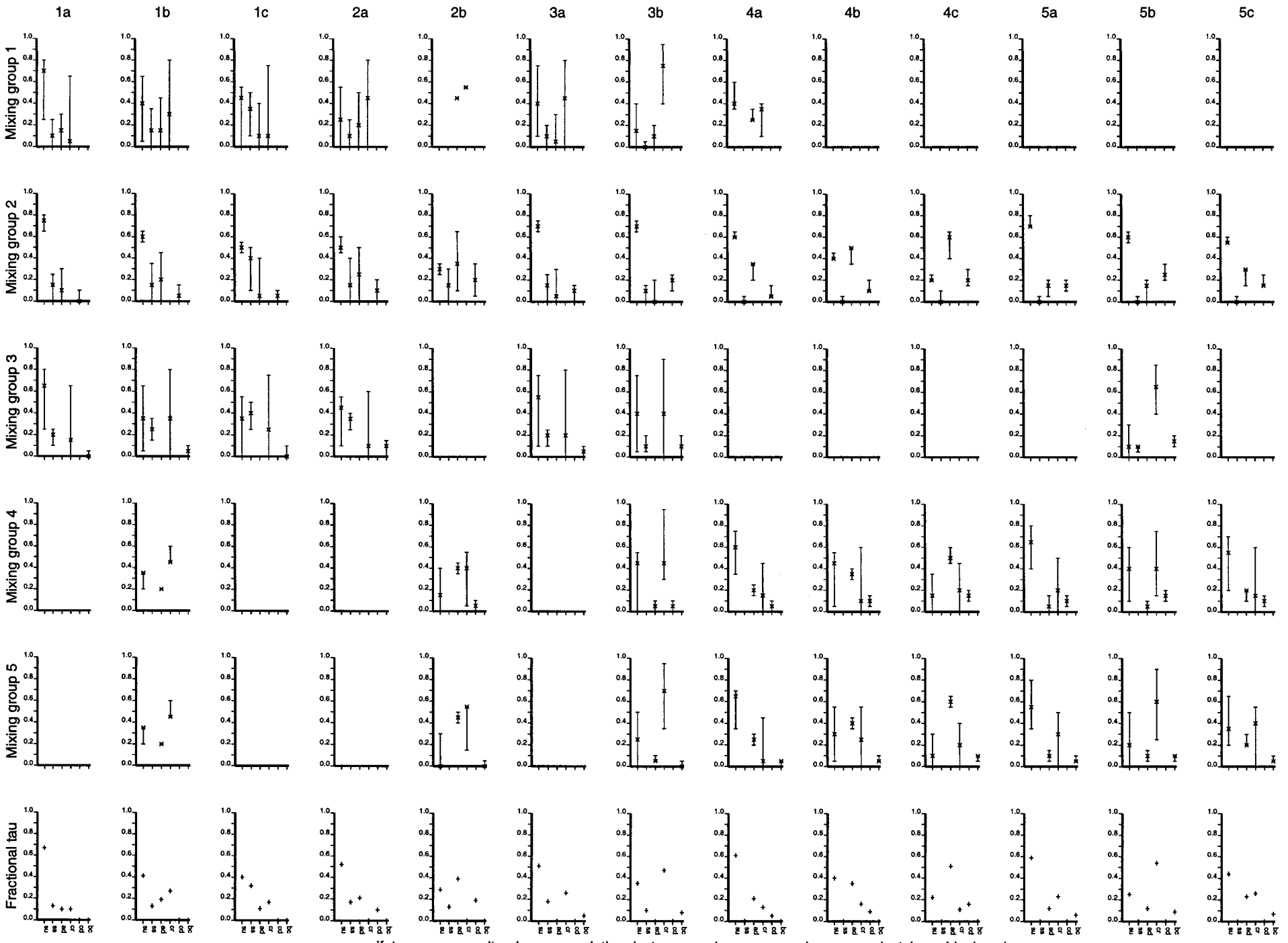

su := sulfate; ss := sea salt; ad := accumulation dust; cr := carbonaceous; cd := coarse dust; bc := black carbon

tau_atm = 0.20, tau_comp = 0.20, mu0 = 0.6

Fig. 4

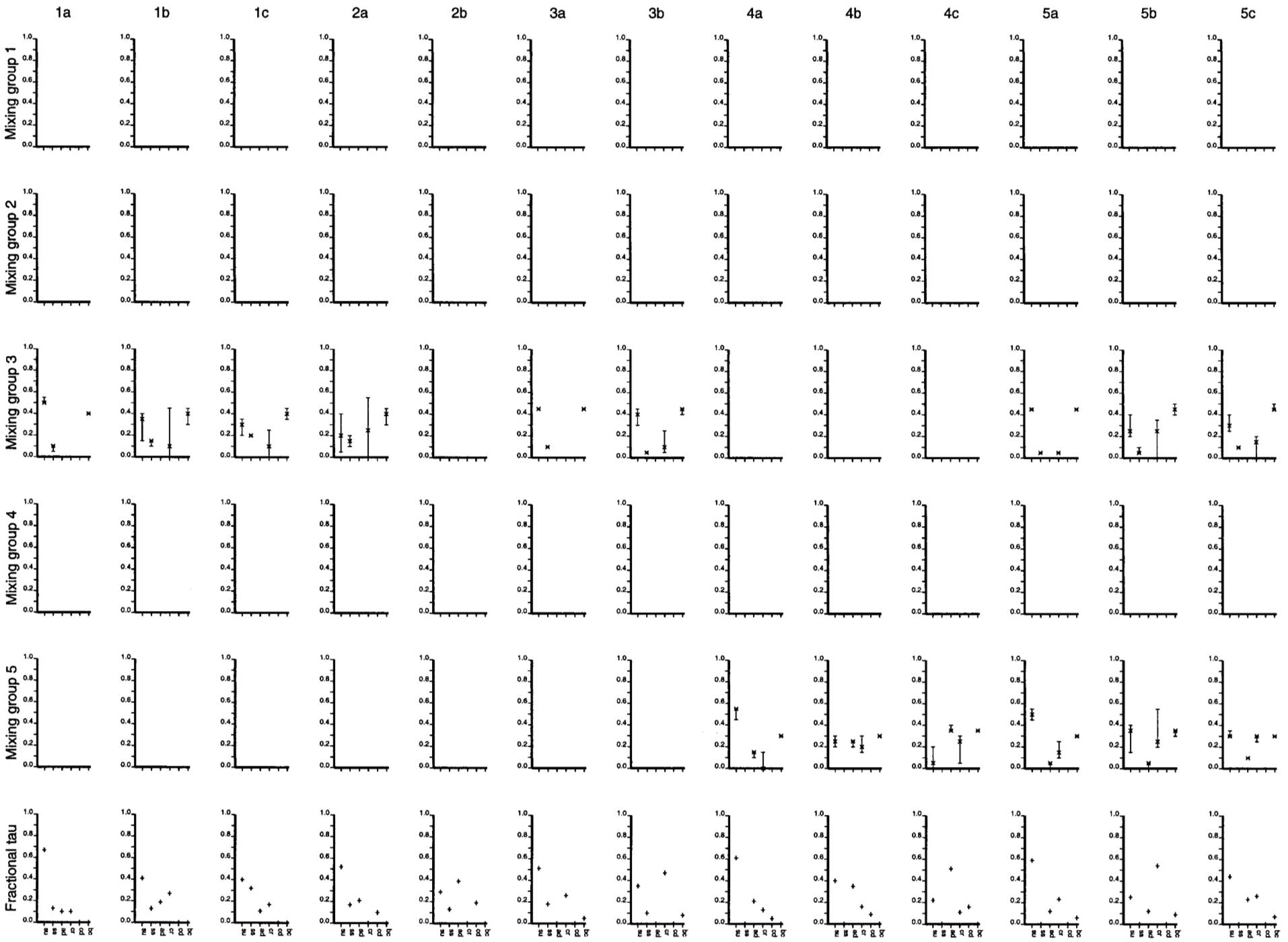
1a
1b
1c
2a
2b
3a
3b
4a
4b
4c
5a
5b
5c
Mixing group 1
Mixing group 2
Mixing group 3
Mixing group 4
Mixing group 5
Fractional tau
su := sulfate; ss := sea salt; ad := accumulation dust; cr := carbonaceous; cd := coarse dust; bc := black carbon
tau_atm = 0.20, tau_comp = 0.30, mu0 = 0.6

Fig. 5

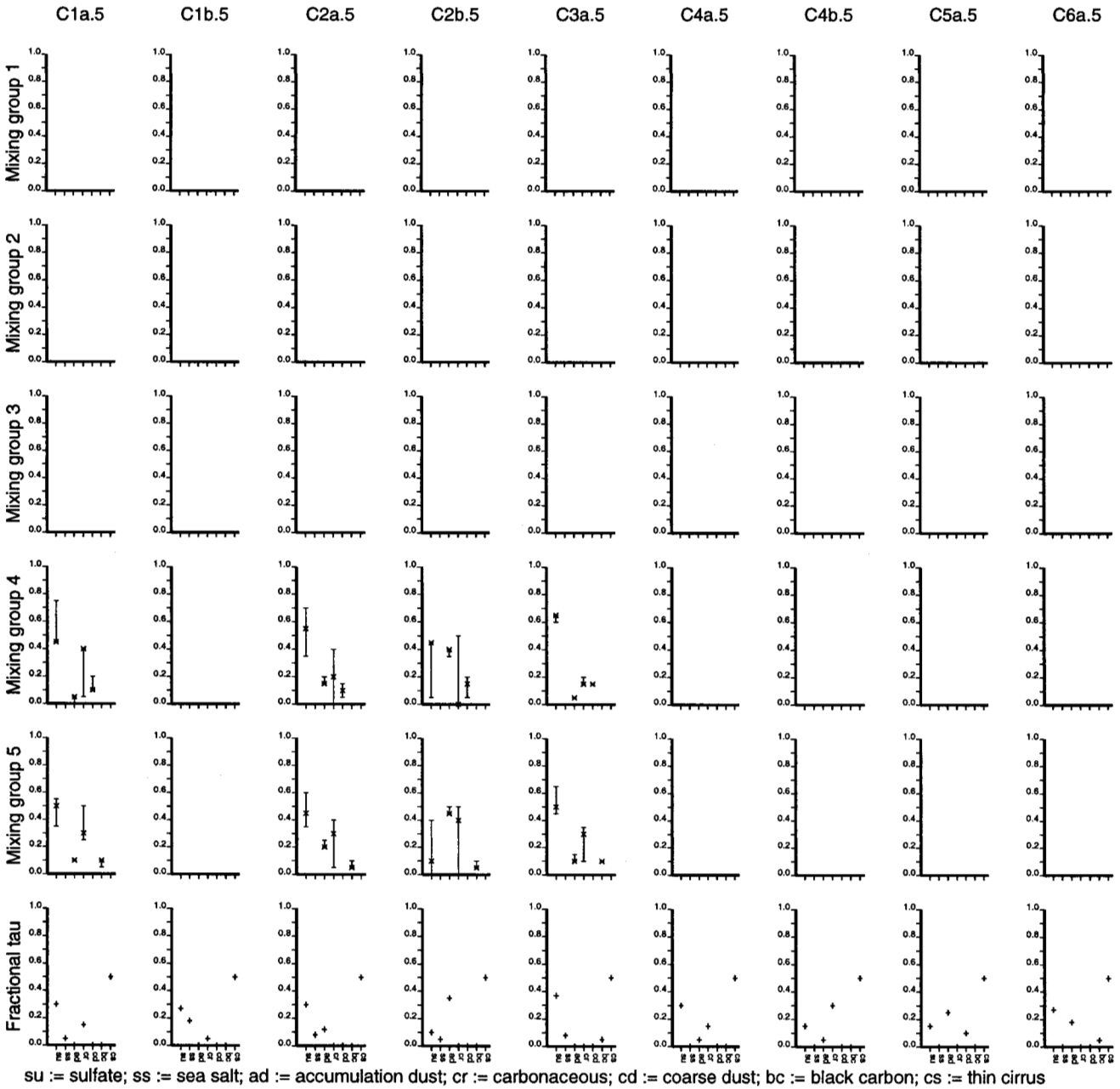

tau_atm = 0.50, tau_comp = 0.50, mu0 = 0.6

Fig. 6

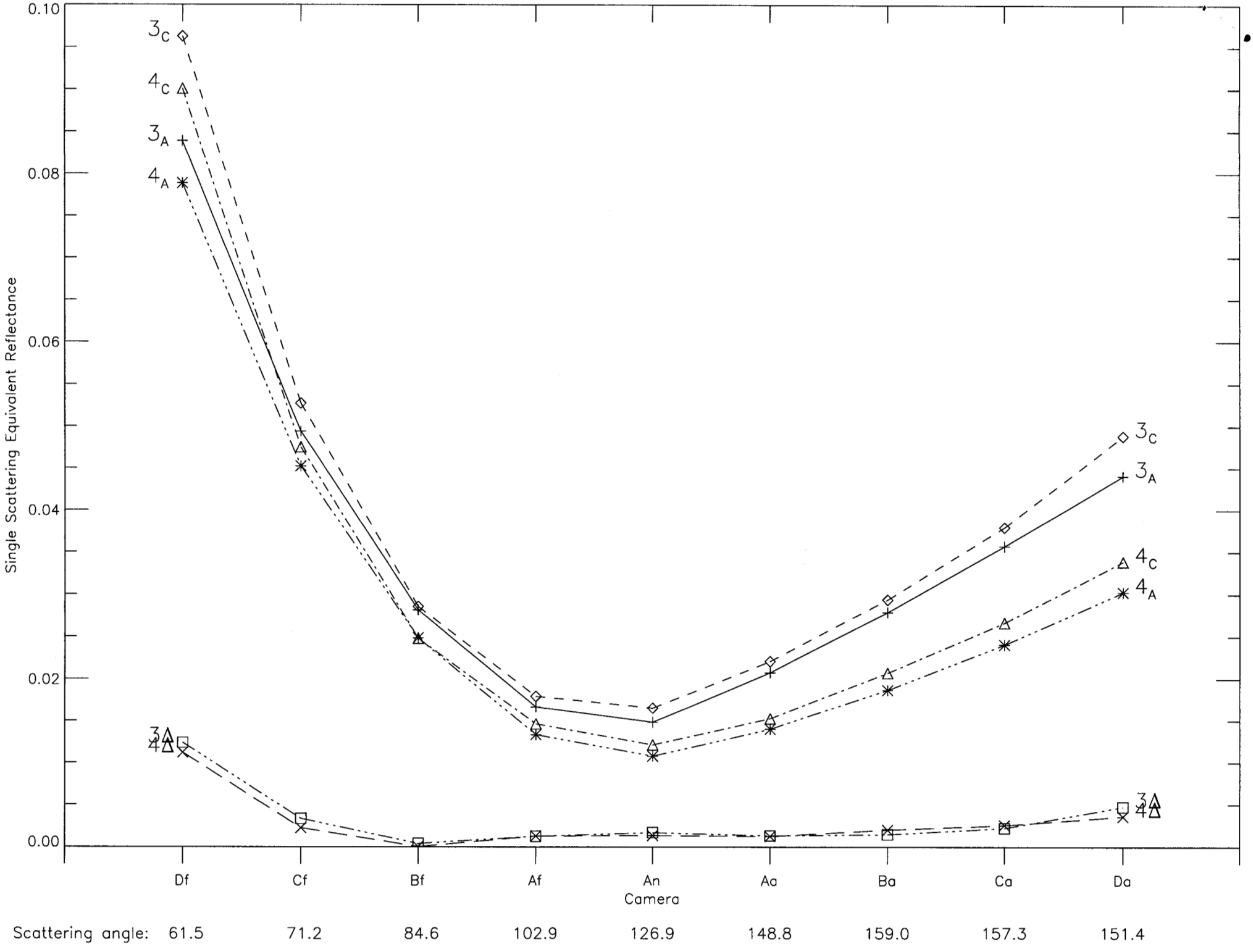
0.10
0.08
0.06
0.04
0.02
0.00
Single Scattering Equivalent Reflectance
3C
4C
3A
4A
Df
Cf
Bf
Af
An
Aa
Ba
Ca
Da
Camera
Scattering angle: 61.5 71.2 84.6 102.9 126.9 148.8 159.0 157.3 151.4

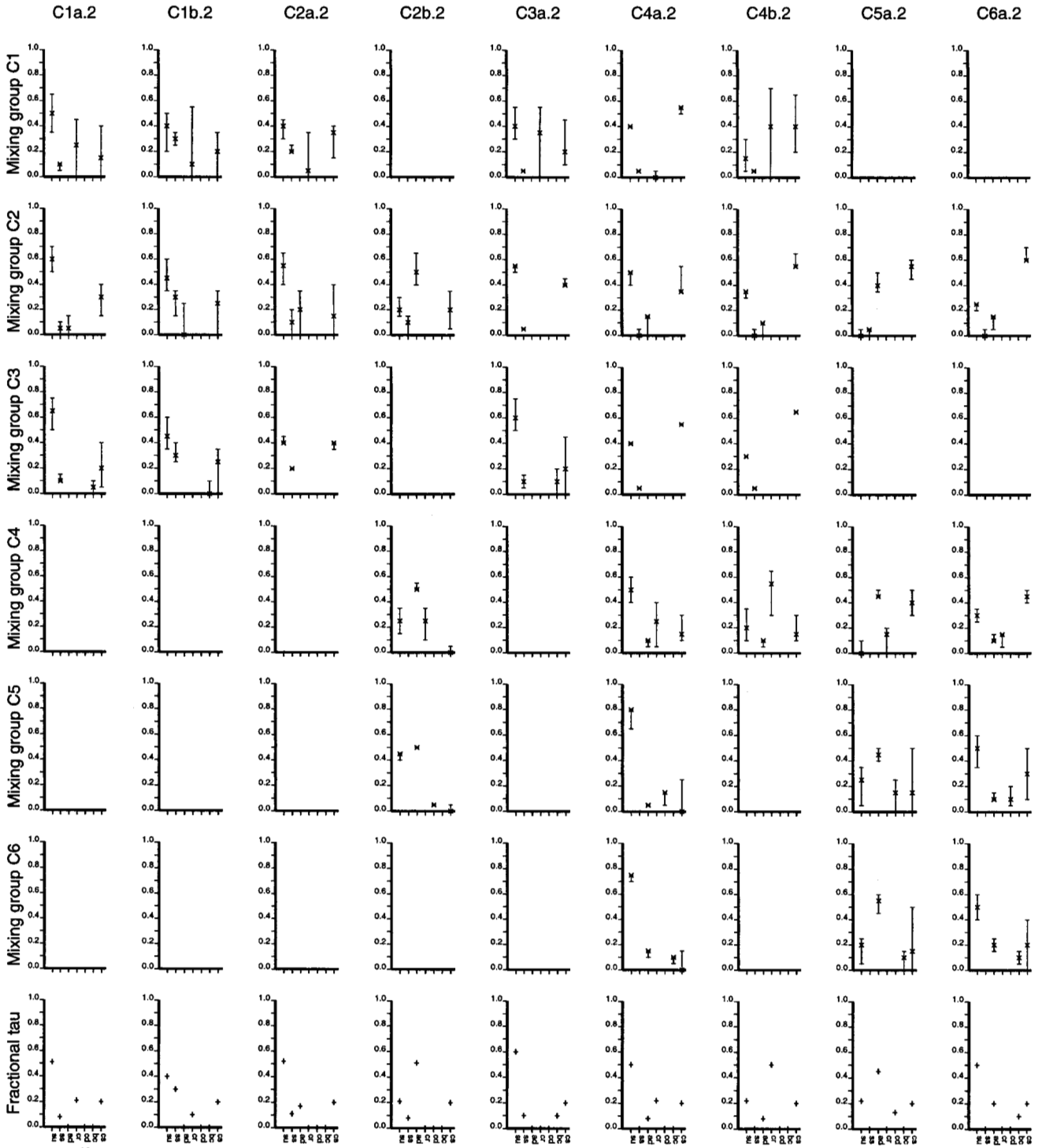

su := sulfate; ss := sea salt; ad := accumulation dust; cr := carbonaceous; cd := coarse dust; bc := black carbon; cs := thin cirrus

tau_atm = 0.50, tau_comp = 0.50, mu0 = 0.6

Fig. 8